# Cellular and Regional Vulnerability Shapes the Molecular Landscape of Psychosis in Alzheimer's Disease

Matheus B. Victor [1,6,8], Na Sun [2,3,7,8], Kyriakitsa Galani [2,3], Noelle Leary [1], Yosuke Tanigawa [2,3], Aine Ni Scannail [1], Li-Lun Ho [2,3], Shaniah Prosper [1], Liwang Liu [1], Julia K. Kofler [4], Robert A. Sweet [5,9], Li-Huei Tsai [1,3,9] & Manolis Kellis [2,3,9]

1. Picower Institute for Learning and Memory, Massachusetts Institute of Technology, Cambridge, MA, USA; Department of Brain and Cognitive Sciences, Massachusetts Institute of Technology, Cambridge, MA, USA.
2. MIT Computer Science and Artificial Intelligence Laboratory, Cambridge, MA, USA.
3. Broad Institute of MIT and Harvard, Cambridge, MA, USA.
4. Department of Pathology, University of Pittsburgh, Pittsburgh, PA, USA.
5. Center for Neuroscience and Department of Psychiatry University of Pittsburgh, Pittsburgh, PA, USA.
6. Current Address: Department of Neuroscience, Icahn School of Medicine at Mount Sinai, New York, NY, USA.
7. Current Address: Whitehead Institute, Cambridge, MA, USA.
8. These authors contributed equally.
9. Corresponding authors.

## Highlights

- Cell-type- and brain-region-specific transcriptional changes in AD with psychosis (AD+P)
- Upper-layer pyramidal dysfunction and metabolic vulnerability marks the pathophysiology of AD+P
- Circuit wiring programs are evoked in AD+P as maladaptive compensatory responses
- AD+P-associated IL-6 signaling impairs neuronal network function in brain organoids

## Abstract

Approximately 40% of Alzheimer's disease (AD) patients develop psychosis, yet the molecular and cellular processes that govern the manifestation of psychotic symptoms in dementia remain

poorly understood. To define the neurobiological correlates that distinguish AD patients with psychosis (AD+P) from AD patients that never exhibited psychotic symptoms (AD-P), we performed single-nucleus transcriptome and epigenome profiling from prefrontal cortex and hippocampus of 48 postmortem brains from AD subjects segmented by psychiatric diagnosis. Our snRNA-seq profiling uncovered differentially expressed genes (DEGs) across multiple cell types, including transcriptional signatures of enhanced synaptic transmission in upper-layer pyramidal neurons of the AD+P cortex. Cell fraction analysis and histology both indicate greater loss of upper-layer pyramidal neurons in AD+P in comparison to AD-P cortex. Integrating our snRNA-seq data with functional screens in stem-cell derived brain organoids, we defined how genetic perturbations modify input-output network connectivity *in vitro* in a model of cortico-cortical communication. We find that differential vulnerability of pyramidal neurons in AD+P is associated with CDK5/p35-associated neurotoxicity and IL6-mediated glial inflammatory expression changes. This neuronal response is associated with microglial exhaustion and astrocytic inflammation signatures triggered by layer-specific neuropathological changes in the brains of AD+P patients. Lastly, we elucidate common and distinct transcriptional signatures between psychosis in AD and several other psychiatric conditions, and found significant enrichment of schizophrenia genetics with AD+P that is most convergent in upper-layer pyramidal neurons. Our work provides novel insight into the pathophysiological role of hyperexcitable circuits in the etiology of neuropsychiatric symptoms of AD.

## Introduction

Alzheimer's disease (AD) is characterized by progressive memory loss, language deficits, impaired cognitive abilities, and behavioral disturbances, all of which severely compromise an individual's ability to perform daily activities[1–3]. Hallmark pathological features of AD include the accumulation of amyloid-beta plaques and tau neurofibrillary tangles, accompanied by glial inflammation and reductions in brain volume, particularly within the hippocampus and prefrontal

cortex, regions integral to memory formation and executive functions[4,5]. These molecular and structural alterations are often preceded by changes in brain activity patterns, detectable through neuroimaging techniques, which manifest within regions harboring early pathological accumulations long before clinical symptoms arise[6].

Therapeutic efforts in AD have predominantly focused on mitigating cognitive decline. However, current pharmacological treatments offer limited efficacy in halting or reversing cognitive impairment[7]. Given the complex and multifactorial nature of AD, it is essential to consider alternative therapeutic targets beyond cognition, particularly those that address non-cognitive symptoms of AD like psychosis, which includes hallucinations and delusions[8]. Mitigating these symptoms may significantly enhance the quality of life for patients and alleviate the burdens faced by caregivers, presenting a more attainable clinical goal compared to reversing advanced cognitive decline in individuals with dementia.

Alzheimer's disease with psychosis (AD+P) is associated with accelerated cognitive deterioration, a heightened burden of tau pathology, pronounced neurodegeneration, and increased mortality risk[9]. Alarmingly, current antipsychotic treatments are accompanied by a black box warning due to a documented rise in fatal outcomes, underscoring the urgent need for novel and effective therapeutic strategies[10,11]. Despite the high prevalence and severe impact of psychosis in AD[12], the underlying neurobiological mechanisms remain poorly understood. Genetic studies of AD+P suggest a common neurobiological pathway rather than nonspecific consequences of widespread neurodegeneration[13–16]. Moreover, emerging evidence implicates the glutamatergic system in the development of a number of psychotic disorders, particularly through neuronal hyperactivity and resultant disruptions in functional connectivity[17,18]. Neuropsychiatric symptoms in AD, including psychosis, have been linked to altered neural circuitry and synaptic dysfunction[19,20], potentially stemming from maladaptive compensatory mechanisms in response to progressive neurodegeneration[21,22].

76 In this study, we utilized single-nucleus RNA sequencing (snRNA-seq) and single-nucleus assay
77 for transposase-accessible chromatin sequencing (snATAC-seq) to investigate the cellular and
78 molecular landscape associated with psychosis in AD. Our analyses reveal that surviving
79 excitatory pyramidal neurons in the upper cortical layers of AD+P brains re-engage
80 developmental genetic programs aimed at circuit assembly, perhaps as an attempt to remodel
81 network connectivity amid ongoing neurodegeneration. Surprisingly, data from stem-cell-based
82 models indicate that these compensatory responses may inadvertently exacerbate
83 neurodegenerative pathology and network dysfunction, offering new insights into the paradoxical
84 nature of neuronal plasticity in AD+P.

85 ## Results

86 ### 1. snRNA-seq atlas of PFC and hippocampus in Alzheimer's disease with and without
87 psychosis

88 To investigate molecular and cellular differences in AD individuals with and without psychosis
89 (AD+P vs. AD-P), we performed single-nucleus RNA-seq (snRNA-seq) on the prefrontal cortex
90 (PFC) and anterior hippocampus (AH) from 24 AD+P and 24 AD-P individuals (**Methods and**
91 **Patient Manifest in Supplementary Table S1**). After quality control, we obtained 160,875
92 transcriptomes, identifying major cell types, including excitatory neurons, inhibitory neurons,
93 astrocytes, oligodendrocytes, oligodendrocyte progenitor cells (OPCs), microglia, vascular cells,
94 and ependymal cells (**Fig. 1A**, **Methods**). Cell types were annotated based on canonical marker
95 gene expression (**Fig. 1B**), and we further classified subtypes within excitatory and inhibitory
96 neurons (**Fig. 1A**). Excitatory neuron subtypes were transcriptionally distinct by cortical layers
97 and brain regions, while inhibitory neuron subtypes were distinguishable based on marker gene
98 expression (**Fig. 1A**).

99 We then assessed whether specific cell type proportions differed between AD+P and AD-P
100 individuals, accounting for confounding factors such as sex, age, and postmortem interval (PMI)

101 (**Methods**). In the PFC, we found that excitatory and inhibitory neurons showed significantly
102 reduced proportions in AD+P, while OPCs were significantly increased in cortex (**Fig. 1C**). At the
103 subtype level, we observed that cortical layer L2 and L3 (ExL2/3) and layers L3 and L4 (ExL3/4)
104 excitatory neurons were disproportionately reduced in AD+P, suggesting cortical layer-specific
105 neuronal loss associated with psychosis in AD (**Fig. 1D**). These correlates are based on marker
106 gene expression that span layers 2 to 4 (L2-L4), suggesting that upper-layer excitatory pyramidal
107 neurons may show differential vulnerability in AD+P. To confirm these findings based on high-
108 throughput sequencing, we performed histology with immunohistochemistry (IHC) in a separate
109 cohort consisting of tissue from 20 postmortem human brain PFCs (n= 10 AD+P versus 10 AD-
110 P) (**Fig. 1E-H, Supplementary Table 2**). Images were segmented into layers based on nuclei
111 density with the marker DAPI. Our histology analysis revealed consistent findings to our snRNA-
112 seq cell fraction analysis, with AD+P subjects showing decreased density of neurons in upper
113 cortical layers L2, L3 and L4, based on the expression of the pan-neuronal marker, NeuN (**Fig.
114 1E**). Neurons in deeper layers (i.e. L5 and L6) were not significantly altered between AD+P and
115 AD-P. To understand how the distribution of pathology across the cortex correlates with neuronal
116 loss, we quantified amyloid-beta plaques and hyperphosphorylated neurofibrillary tau tangles
117 (NFTs) across PFC brain tissue (**Fig. 1F-H**). Numerous postmortem studies have reported that
118 AD+P subjects exhibit greater NFT burden, while less consistent changes have been described
119 for the levels of amyloid plaques[23–25]. We found that the density of amyloid plaques with the
120 amyloid probe Methoxy-X04 are greater in upper cortical layers (L1-L4) and reduced in deeper
121 layers (L5 and L6) across all subjects, suggesting upper cortical neurons bear greater plaque
122 burden (**Fig. 1F)**. Nevertheless, comparisons of amyloid densities segmented by psychosis
123 presence (i.e. AD+P versus AD-P) did not show significant changes. When segmented by cortical
124 layers, L4 showed a trend for increased plaques in AD+P (p-value = 0.09 with two-way ANOVA
125 with bonferroni post hoc test) (**Fig. 1F and Supplemental Fig. S1A**). Next, we assessed if the
126 levels of Tau phosphorylation (pTau), which is the main substrate of NFTs, were significantly

127 altered in postmortem PFC brain tissue of AD+P relative to AD-P samples (**Fig. 1F)**. Although the
128 pattern of the distribution of pTau across the cortex were seemingly distinct between the two
129 groups, we did not find statistically significant changes in specific cortical layers, but an overall
130 increase across all layers (**Fig. 1F and Supplemental Fig. S1A**). These results suggest that
131 neuropathological changes do not drive the differential vulnerability of upper cortical neurons in
132 AD+P. However, our results do not rule out the possibility that neuropathological changes may
133 act as a trigger to neuronal susceptibility. Of note, we did not find significant differences in the cell
134 proportions of the AH (**Supplemental Fig. S2**). Although the mechanism at play remains
135 unknown, we reasoned that transcriptional programs may reveal the differential responses in
136 AD+P that lead to the relative greater loss of upper cortical neurons.

137 **2. Cell-type- and brain-region-specific transcriptional changes in AD with psychosis**

138 We next examined transcriptional changes in AD+P versus AD-P individuals by performing
139 differential gene expression analysis for each cell type and brain region. Using MAST (single-cell
140 level) and EdgeR (pseudo-bulk level), we obtained consistent results across methods
141 (**Supplemental Fig. S3A-B, Methods**). In PFC, we identified 1,534 upregulated and 1,416
142 downregulated genes in AD+P individuals, with high cell-type specificity (**Fig. 2A, Supplemental**
143 **Table 3**). In the hippocampus (AH), we found 576 upregulated and 540 downregulated genes
144 (**Fig. 2B, Supplemental Table 4**), fewer than in the PFC, suggesting more dramatic
145 transcriptional changes in the PFC at the time of sample collection.

146 We systematically compared DEGs between the two regions and categorized them into six
147 groups: shared upregulated, AH-specific upregulated, PFC-specific upregulated, shared
148 downregulated, AH-specific downregulated, and PFC-specific downregulated. Gene expression
149 changes showed consistent trends across regions, even with varying significance levels (**Fig. 2C**).
150 Notably, the PFC had more region-specific DEGs in excitatory neurons, inhibitory neurons, and
151 astrocytes, while the hippocampus showed higher microglia-specific DEGs. These findings

152 suggest more severe neuronal loss in the PFC, consistent with the cell proportion analysis (**Fig.**
153 **1C**), and stronger microglia-driven inflammation in the hippocampus in AD+P individuals.

154 To explore the biological functions of DEGs in these six groups, we performed gene ontology
155 (GO) enrichment analysis for each cell type (**Fig. 2C, Supplemental Fig. S4, Methods**). In
156 excitatory neurons (**Fig. 2D**), we found that shared upregulated genes were enriched in protein
157 unfolding and synaptic vesicle endocytosis. Hippocampus-specific upregulated genes were linked
158 to protein folding and JUN kinase activity, while PFC-specific upregulated genes were associated
159 with synapse organization, neuron projection regulation, and neuron death. Shared
160 downregulated genes were involved in cell cycle signaling and glucose starvation response, while
161 PFC-specific downregulated genes showed enrichment in cilium organization and extracellular
162 transport. These results highlight distinct and shared functional pathways in the PFC and
163 hippocampus, emphasizing region-specific mechanisms in AD+P individuals.

164 Our cell fraction analysis and transcriptional results likely reflect the regional impact of AD
165 progression, with more severe neurodegenerative phenotypes in AH than PFC[26]. Notably, our
166 snRNA-seq profiling data was derived from subjects with an average age at death of 86 years old
167 (ranging from 65 to 102 years old and balanced between AD+P and AD-P). Adding further support
168 to the notion that disease progression may hinder our ability to uncover early pathological triggers,
169 particularly as it relates to AH. It is also possible that the neural substrates that drive psychosis
170 are indeed more dependent on cortical than hippocampal processes, particularly as it pertains to
171 AD patients with or without psychosis. Nevertheless, due to the salience of our results in the PFC,
172 we decided to focus on these processes to further derive mechanistic insights into the neural
173 substrates that drive the manifestation of psychotic symptoms in dementia.

174 **3. Compensatory mechanism evoked by surviving excitatory neurons in PFC.**

175 Neuronal DEGs in the PFC are particularly striking for pathways related to metabolic processes.
176 This includes GO terms associated with up-regulated genes that relate to glycolysis, mitochondrial

177 respiration, mitochondrial membrane remodeling and mitochondrial apoptotic signaling
178 (**Supplemental Figure S5** and **Supplementary Table S5**). Along with these transcriptional
179 programs that may suggest metabolic dysfunction across a wide range of neuronal subtypes,
180 excitatory neurons also exhibit up-regulated terms related to synaptic transmission,
181 neurotransmitter signaling, neuronal development and neuronal projection morphogenesis. To
182 define the relative enrichment of these synaptic-related DEGs, we curated the genes from these
183 GO terms and mapped their expression across cortical layers. Here, we stratified their relative
184 enrichment by cortical laminae based on the co-expression of layer-specific markers. We found
185 that synaptic-related DEGs were mostly enriched in upper cortical layers L2 and L3 (**Fig. 3A**).
186 This initial finding was counterintuitive, given that based on cell fraction analysis and histology we
187 identified a significantly lower number of neurons in cortical layers L2 and L3 of the AD+P brains.
188 We hypothesized that the upregulation of synaptic and neuronal transmission genes may rather
189 reflect a compensatory mechanism by surviving neurons in the face of neurodegeneration. To
190 test this idea, we probed PFC human brain sections from AD+P and AD-P subjects with
191 fluorescent in situ RNA hybridization using an RNAscope probe for synapsin 1 (SYN1), an AD+P
192 up-regulated DEG which encodes a critical neuronal protein well-known to regulate
193 synaptogenesis and neurotransmitter release[27] (**Fig. 3B**). Notably, SYN1 is robustly and
194 restrictively expressed by neurons[28]. Our analysis revealed that the number of RNAscope dots
195 per nucleus for a given SYN1-positive neuron (comprising at least 3 SYN1 dots) increased in
196 AD+P (**Fig. 3C and 3D**). While these results were only significantly increased in L2 and L3, deeper
197 layers also showed trends for increased SYN1 RNAscope dots. In agreement with our previous
198 observations, the overall percentage of cells positive for SYN1 in cortical layers L2 and L3 were
199 significantly reduced (**Fig. 3E**). From these experiments we concluded that the relatively greater
200 expression of this synaptic-related transcriptional signature in AD+P PFC captured by our snRNA-
201 profiling is indicative of a compensatory mechanism by surviving neurons, perhaps in an attempt

202 to maintain circuit function and integrity. Nevertheless, it remains unclear from these observations
203 what are the impact of these genetic programs on the function of neural circuits.

204 The balance between excitation and inhibition (E/I) is tightly regulated in the adult cortex[29].
205 Disturbances to E/I balance are linked to many neuropsychiatric disorders, including
206 schizophrenia [30]. The association between schizophrenia and E/I disturbances has been
207 implicated particularly with changes in the activity of Parvalbumin (PV) interneurons[31–33]. PV
208 interneuron's fast-spiking properties and fast GABA release are thought to be critical in shaping
209 the activity of cortical ensembles and network synchrony[34]. PV-expressing interneurons can be
210 divided into several subpopulations, with the most prominent being basket cells[35]. In our snRNA-
211 seq analysis, PV basket cells are significantly decreased in AD+P, with DEGs indicative of
212 widespread metabolic dysfunction (**Fig. 3F and 3G**). Lack of balance in the ratio of excitatory to
213 inhibitory neurons or perturbations in the activity of inhibitory neurons can greatly modify the
214 output of excitatory neurons[36]. Although enhanced glutamatergic signaling has been previously
215 implicated in psychosis[17,18], many studies have also reported through functional imaging that AD
216 patients with psychotic symptoms have reduced correlates of neuronal activity[8]. Hence, the
217 functional consequence of our snRNA-seq results to circuit function is uncertain. Next, we decided
218 to explore the functional impact of the gene expression perturbations we uncovered in AD+P
219 brains to the activity of neuronal ensembles by employing induced pluripotent stem cell (iPSC)-
220 based models of the human brain.

221 **4. Functional characterization of AD with psychosis DEGs from upper-layer pyramidal**
222 **neurons.**

223 The mammalian neocortex processes signals through local microcircuits that are arranged in
224 distinct layers of information processing pathways[37]. Excitatory pyramidal neurons in layers L2
225 and L3 send long-range axons to distant brain regions, making them essential for cortical
226 information processing[38]. We envisioned building an in vitro platform of cortico-cortical

227 connectivity from which we could infer how genetic perturbations in L2 and L3 of AD+P brains
228 impact circuit function. Human iPSCs patterned to adopt neural fates and forced to grow in 3D
229 form structures known as brain organoids that have become sophisticated tools to model the brain
230 in a human-based context[38,39]. Here, we employed established protocols to generate forebrain
231 organoids[40], composed predominantly of excitatory neurons, that recapitulate major cortical layers
232 to engineer an input-output model of neuronal connectivity.

233 To gain control over neuronal activity patterns, we first generated an iPSC line that constitutively
234 expressed the channelrhodopsin variant CheRiff [41] under the neuronal-restrictive promoter human
235 Synapsin (hSyn-CheRiff). We then differentiated this line into forebrain organoids (**Fig. 4A**) We
236 found that CheRiff and its increased sensitivity to blue light, allowed for faithful control of neuronal
237 activity in organoids with blue light stimulation despite the high refractive index of culture media
238 (**Fig. 4B**). Towards our goal of building a model of cortico-cortical connectivity, we created an
239 assembloid by fusing two forebrain organoids together. Assembloids have been previously used
240 to model connectivity across distinct brain regions, as they allow for organoids derived from
241 multiple iPSC lines or organoids separately patterned to adopt distinct brain regionalities to be
242 assembled post-production [40]. To test the extent to which excitatory neurons in one organoid
243 hemisphere projects across to the contralateral hemisphere, we infected organoids with the
244 axonal-restricted genetically-encoded calcium indicator AAV Axonal-GCaMP6s and later
245 generated assembloids with non-infected organoids[42]. This allowed us to image the activity of
246 neurons whose projections crossed the assembloid junction line and confirm their input to the
247 contralateral side (**Fig. 4C** and **Supplemental Movie S1**).

248 Next, we fused organoids that harbored constitutive Syn-CheRiff expression with organoids
249 previously infected with Synapsin-GCaMP6s to generate assembloids. Here, we would gain
250 optogenetic control of neuronal activity in one hemisphere while having the capability of observing
251 neuronal activity in the contralateral hemisphere via calcium imaging. Using this simple input-

252 output model of neuronal connectivity, we reasoned that we could ectopically express synaptic-
253 related upregulated DEGs from L2 and L3 of AD+P brains to the input hemisphere to probe its
254 impact on the function and connectivity of neural circuits (**Fig. 4D**). In our model, optogenetic
255 stimulation produced large amplitude calcium events on the contralateral organoid **(Fig. 4E, Fig.**
256 **4F, and Supplemental Movie S2**). We curated 37 genes upregulated in AD+P L2/L3 excitatory
257 neurons from GO terms related to neuron projection development (genelist in **Fig. 3A**) and
258 delivered them with lentiviral vectors under a ubiquitous promoter to hSyn-CheRiff organoids at
259 90 days after differentiation. In parallel, a separate set of organoids from the same line and batch
260 that did not carry the hSyn-CheRiff construct were infected with AAV Synapsin-GCaMP6s. On
261 day 120, these two sets of organoids were fused and made into assembloids. Ten days later, we
262 screened activity patterns following stimulation in distinct assembloids in comparison to non-
263 transduced controls (**Supplemental Movie S3**). We ranked the activity of the contralateral
264 organoid based on calcium dynamics and binned them into groups of increased activity (n=9 of
265 DEGs tested), no change (n=10 of DEGs tested), or reduced activity (n=18 of DEGs tested) in
266 comparison to controls (**Fig. 4G**).

267 Given that we chose to ectopically express genes related to neuronal projection development,
268 and that the majority of the DEGs we tested decreased activity on the contralateral organoid, we
269 wondered to what extent these genetic manipulations modify the span of projections across
270 assembloid junctions. Using the stable GFP signal of the hSyn-CheRiff line, we traced
271 fluorescence to the contralateral hemisphere near the vicinity of the assembloid junction and
272 ranked it from least to most projection (**Fig. 4H**). Interestingly, we found instances of DEGs that
273 decreased activity on the contralateral organoid but counterintuitively increased projections
274 across the assembloid junction. One such example is CAMK2B, a gene that encodes the beta
275 subunit of the calcium/calmodulin-dependent protein kinase II and plays a critical role in synaptic
276 plasticity and dendritic arborization[43]. In experiments overexpressing CAMK2B or an identical

277 construct but that instead carried the blue fluorescent protein EBFP, we found that CAMK2B
278 overexpression leads to enhanced vulnerability of neurons following optogenetic stimulation
279 compared to controls, likely due to excitotoxicity (**Supplemental Figure S6**). In fact,
280 overexpression of CaMKII has previously been shown to increase glutamate-induced neuronal
281 death in similar contexts[43,44]. While the overexpression of CDK5R1, an AD+P L2/L3 upregulated
282 DEG, led to similar phenotypes as CAMK2B overexpression (i.e. less contralateral activity but
283 more projection across assembloid junction), we did not find evidence of enhanced excitotoxicity
284 (**Fig. 4H** and **Supplemental Figure S6**). CDK5R1 encodes for a protein known as p35, a neuron-
285 specific activator of the cyclin-dependent kinase 5 (CDK5)[45]. While the activation of CDK5 is
286 required for proper central nervous system development and cortical lamination [45,46], CDK5 is also
287 a key enzyme responsible for the phosphorylation of tau[47]. Of note, p35 can be proteolytically
288 cleaved by excitotoxic triggers such as amyloid beta aggregation or high levels of intracellular
289 calcium to generate a smaller peptide known as p25[48,49]. Interestingly, the p25 form of this protein
290 has been shown to accumulate in neurons of patients with AD[50]. Since p25 has been shown to
291 increase CDK5 kinase activity, it is thought that this could be a critical mechanism linking disease-
292 associated toxic events to neuronal tau hyperphosphorylation and the pathological formation of
293 NFTs[51]. In mice, CDK5R1 peaks in expression during early development where it plays a crucial
294 role in promoting neurite outgrowth[51,52], congruent with our observation of greater projections
295 across the assembloid junctions in CDK5R1 overexpressing organoids. Since we observed
296 decreased activity on the contralateral organoid, we decided to test the impact of CDK5R1
297 overexpression on the infected organoid itself. We found that CDK5R1 overexpression
298 dramatically decreased levels of neuronal activity in infected organoids two weeks post-
299 transduction (**Fig. 4I and 4J**).

300 To determine the integrity of the neurons following CDK5R1 overexpression, we fixed and
301 performed immunostaining on infected organoids derived from a healthy control subject cultured

302 for over 18 months. Staining for the neuronal marker MAP2 showed neuronal processes that were
303 free of blebbing with intact morphologies (**Fig. 4K**). We probed pTau at a known Cdk5
304 phosphorylation site, Ser396 [53], in CDK5R1 overexpressing or EBFP-infected organoids and
305 found a robust increase in the levels of pTau with CDK5R1 overexpression (**Fig. 4K**). It is
306 important to also note that many of the Cdk5 target sites are hyperphosphorylated in post-mortem
307 AD brain samples[51]. IHC with pTau Ser396 antibody in a cohort of postmortem human brain PFCs
308 also revealed increased levels of pTau in AD+P compared to AD-P subjects (n= 10 AD+P versus
309 10 AD-P) (**Fig. 4L**). Notwithstanding, this study and others have reported that overall levels of
310 pTau are increased in AD+P, and not only in a phosphorylation site-specific manner[23].
311 Collectively, our experimental data suggests a compensatory mechanism by pyramidal cells in
312 AD+P that may ultimately disrupt network connectivity and exacerbate neuropathology. Notably,
313 many functional imaging studies to date have reported that AD patients with neuropsychiatric
314 symptoms have decreased gray matter volume and reduced network connectivity [54].
315 Nevertheless, the molecular and cellular cues that evokes these genetic programs in AD+P
316 excitatory upper-layer neurons leading to their preferential vulnerability remains unclear.

317

318 **5. Glial response in AD with psychosis is marked by microglial exhaustion and astrocyte-**
319 **driven inflammation.**

320 Next we sought to explore how transcriptional programs in glia may reflect our findings of neuronal
321 vulnerability in the AD+P cortex. We were particularly interested in exploring the crosstalk of
322 astrocytes and microglia, as the most significant pathways for DEGs in each cell type suggested
323 enrichment of an inflammatory signaling axis. Up-regulated DEGs for astrocytes include GO terms
324 for “cellular response to cytokine stimulus” while up-regulated DEGs for microglia include
325 “cytokine-mediated signaling pathway” (**Fig. 5A** and **Supplemental Table S6**). Microglial
326 transcriptional programs in response to aging and AD have been previously deeply characterized

327 with snRNA-seq from mouse models of neurodegeneration and postmortem human brains[55–59].
328 While a wide variety of transcriptional programs associated with disease states have been
329 catalogued, microglial activation across disease is consistently marked by the downregulation of
330 a handful of homeostatic gene markers. One such case is the loss of P2RY12 expression, a
331 purinergic receptor thought to mediate microglial surveillance[60]. Even though our cell fraction
332 analysis did not capture any significant changes in microglial content between AD+P and AD-P
333 brains (**Fig. 1A**), we attempted to determine via immunohistochemistry if the coverage of
334 P2RY12-positive microglial processes were changed between AD+P and AD-P subjects. Our
335 analysis did not find significant changes (**Fig. 5B**), suggesting that microglia number and
336 activation status is similar across AD independent of neuropsychiatric diagnosis. At closer
337 inspection, up-regulated DEGs of microglia revealed a widespread genetic program reflective of
338 cellular response to stress (e.g. unfolded proteins and heat shock proteins) (**Fig. 5C** and
339 **Supplemental Table S6**). Additionally, upregulated DEGs include PLCG2, whose expression
340 increases in plaque-associated microglia[61], suggesting that perhaps AD+P stress-induced
341 microglial states could be triggered by neuropathology burden. Moreover, AD+P microglia
342 differentially upregulated canonical markers of inflammation, such as JAK-STAT pathway (e.g.
343 JAK3 and STAT3[62]). Interestingly, upregulation of stress and inflammatory programs in AD+P
344 microglia is also accompanied by well-established markers of cellular senescence (i.e. CDKN1A
345 which encodes the protein p21)[63] (**Supplemental Table S6**). Many reports have now identified
346 that exposure to tau is a potent inducer of microglial senescence[64,65]. Hence in the AD+P cortex,
347 microglia adopt an exhausted state that is marked by pro-inflammatory programs, possibly
348 reflecting a maladaptive response to persistent stress signals in the local microenvironment. This
349 may represent a decoupling of classical neuropathology burden from immune cell activation,
350 where microglia respond to subtle cues, such as altered synaptic function or tau pathology, rather
351 than overt plaque deposition.

352 While our cell fraction analysis did not capture changes in astrocytic content between AD+P and
353 AD-P brains, there was a non-significant trend for increased numbers of astrocytes in AD+P
354 subjects (**Fig. 1A**), which was similarly the case through histology of cortical gray matter using
355 the astrocyte marker GFAP (**Fig. 5D**) (n= 10 AD+P versus 10 AD-P; p-value = 0.076, student's t-
356 test). Using the nuclear stain DAPI to parse cortical layers, our quantification of astrocytes across
357 the cortical gray matter revealed greater levels of GFAP specifically in layer L2 of AD+P brains
358 (**Fig. 5E**). To further define the astrocytic response, we attempted to identify the master regulators
359 of this transcriptional program and build a Transcriptional Regulatory Network (TRN)[66]. Here, we
360 used the top GO term related to the up-regulated DEGs of "cellular response to cytokine stimulus"
361 and found that STAT3 showed the greatest enrichment for transcription factors (TFs) (**Fig. 5F**).
362 Of note, we found that STAT3 itself is upregulated in astrocytes of AD+P versus AD-P subjects
363 (**Supplemental Table S6**). To confirm this finding, we probed PFC human brain sections from
364 AD+P and AD-P subjects with fluorescent in situ RNA hybridization using RNAscope probes for
365 STAT3 and GFAP (**Fig. 5G**). Using this approach, we first defined astrocytes as cells bearing at
366 least 3 GFAP RNAscope dots, and subsequently mapped the percent of these cells that were
367 also double positive for STAT3. We focused this analysis specifically on layers L2 and L3 since
368 we had seen greater GFAP signal in the proximity of this cortical region in AD+P brains. Our
369 results identified a robust increase in the presence of STAT3 expression in AD+P astrocytes,
370 further confirming our snRNA-seq dataset (**Fig. 5G**).

371 To define the cellular signaling pathways that drive this response, we imputed the same list of up-
372 regulated DEGS into the Pathway Interaction Database (PID)[66] and found that IL6-mediated
373 signaling is the major driver of this STAT3 astrocytic response (**Fig. 5H**). IL-6 (Interleukin-6) is a
374 pleiotropic cytokine involved in the activation of the transcription factor STAT3 through JAK/STAT
375 signaling[67]. Of interest, the IL6ST, a gene that encodes a critical interleukin 6 cytokine family
376 signal transducer[67,68], is also up-regulated in AD+P astrocytes (**Supplemental Table S6**). In the

377 brain, IL-6 is largely produced by activated astrocytes and microglial cells[69]. Furthermore,
378 aberrant IL-6 signaling is known to lead to neuronal dysfunction and synaptic loss and therefore
379 to be correlated with cognitive decline and memory impairment in AD[70]. To test the impact of IL-
380 6 signaling to neuronal physiology and CDK5R1 expression, we treated organoids seeded on
381 multielectrode arrays (MEA) with recombinant IL-6 and recorded their activity (**Fig. 5I-5K**). Using
382 organoids derived from our hSYN-CheRiff optogenetic iPSC line, we first tested the ability of
383 optogenetic stimulation to drive population spikes following overnight incubation with 5ng/ml of
384 recombinant IL-6. During a 15 minute recording session, we observed a dramatic decrease in
385 activity in organoids with very few spikes detected upon 10Hz blue stimulation when treated with
386 IL-6 (**Fig. 5I** and **Fig. 5J**). It has been previously reported that IL-6 treated primary mouse neurons
387 accumulate abnormal levels of hyperphosphorylated tau, which is mediated through increased
388 levels of CDK5R1 and its encoded protein p35, the activator of CDK5 [71]. Hence, we tested the
389 expression of CDK5R1 in IL-6 treated organoids and found that indeed suppression of neuronal
390 activity is concomitant with up-regulation of CDK5R1 expression (**Fig. 5K**). Collectively, these
391 results point to a neuroinflammatory axis driven by IL-6 that promotes astrocyte activation and
392 the demise of circuit function.

393 **6. Epigenetic regulation of cell-type-specific gene expression changes and association**
394 **with Schizophrenia genetics**

395 To uncover the epigenetic mechanisms underlying cell-type-specific gene expression changes,
396 we analyzed chromatin accessibility using single-nucleus ATAC-seq (snATAC-seq) from human
397 postmortem brain samples of the same cohort (**Methods**). From 241,430 high-quality nuclei, we
398 identified epigenetic patterns across major brain cell types, including excitatory and inhibitory
399 neurons, astrocytes, oligodendrocytes, OPCs, microglia, and vascular cells, using promoter
400 signals of canonical marker genes (**Fig. 6A, Supplemental Fig. S7A**). Similar to snRNA-seq
401 results, nuclei were clustered primarily by cell identity in UMAP space, regardless of phenotypic

402 group or brain region (**Fig. 6B-C**). Cell proportion analysis revealed fewer neurons in the
403 hippocampus compared to the PFC (**Supplemental Fig. S7B**). Notably, PFC snATAC-seq data
404 captured fewer excitatory neuron nuclei than snRNA-seq data, possibly reflecting epigenetic
405 erosion[72] (**Supplemental Fig. S7C**).

406 To validate cell-type annotation in snATAC-seq, we integrated snRNA-seq and snATAC-seq data
407 for each brain region, in which nuclei from the same annotated cell type clustered tightly together
408 (**Supplemental Fig. S7D-E**). We identified accessible chromatin peaks, annotated their genomic
409 features, and performed GREAT enrichment analysis, which revealed cell-type-specific biological
410 functions (**Fig. 6D, Supplemental Fig. S7F, Supplementary Table S7**). For instance, peaks in
411 excitatory neurons were enriched in synaptic plasticity, trans-synaptic signaling, and ion transport
412 regulation. Inhibitory neuron peaks were enriched in interneuron axon guidance and fate
413 commitment. Astrocyte peaks were linked to Ras signaling and sensory organ development.
414 Oligodendrocyte peaks were associated with myelination and axon ensheathment, while
415 microglial peaks were enriched in immune effector processes and regulation of immune response.
416 These findings demonstrate that cell-type-specific epigenetic patterns reflect functional identities
417 and provide insights into gene expression changes in disease contexts.

418 To explore how epigenetic regulation influences gene expression, we linked distal peaks to
419 promoters using co-accessibility patterns (**Methods**). We identified 158,246 peak-to-promoter
420 links implicating 16,193 genes and 82,695 peaks (**Supplemental Fig. S7G, Supplementary**
421 **Table S8**). Motif analysis on distal peaks associated with differentially expressed genes between
422 AD+P and AD-P individuals identified 171 transcription factors (TFs) regulating DEGs in SF
423 (**Methods**). Additionally, we inferred 94 TFs whose known targets were enriched among DEGs
424 using enrichment analysis. By integrating these approaches with expression of TFs, we identified
425 30 TFs regulating upregulated DEGs in AD+P and 22 TFs regulating downregulated DEGs (**Fig.**
426 **6F-G**). Notably, TFs like FOS, JUND, and JUN were implicated in both upregulated and

427 downregulated DEGs, indicating dual regulatory roles. SPI1, a key microglial TF, was linked to
428 downregulated microglial genes in AD+P, suggesting potential microglial dysfunction.

429 We further investigated how genetics influences downstream gene expression changes. Using
430 Stratified Linkage Disequilibrium Score Regression (S-LDSC)[73], we evaluated the heritability
431 enrichment of AD and schizophrenia genetic variants in accessible peaks linked to DEGs in AD+P
432 (**Methods**). Schizophrenia variants were more associated with AD+P DEGs than AD variants
433 (**Fig. 6H, Supplemental Fig. S8H**), implying a shared genetic basis for psychotic symptoms in
434 AD and schizophrenia. For instance, DEGs in layers 2/3, 3/4, and 4/5 excitatory neurons in AD+P
435 were strongly associated with schizophrenia variants (**Fig. 6H**). Moreover, comparing DEGs
436 across AD vs. controls, AD+P vs. AD-P, and schizophrenia vs. controls revealed shared
437 downregulated DEGs in excitatory neurons between AD+P and schizophrenia (**Fig. 6I,**
438 **Supplemental Fig. S8I-J**). Gene Ontology analysis showed AD+P-specific downregulated DEGs
439 in excitatory neurons were enriched in DNA repair, TOR signaling regulation, and extracellular
440 transport, while upregulated DEGs were linked to gluconeogenesis, neurotransmitter secretion,
441 and autophagy (**Fig. 6J-K**). These findings highlight distinct molecular and cellular responses to
442 psychosis in AD patients.

## 443 Discussion

444 By leveraging single-nucleus transcriptomic and epigenomic profiling of postmortem brains
445 alongside functional validation in stem-cell-derived models, our study highlights the intricate
446 interplay between neuronal circuit function, glial inflammation, and metabolic vulnerability in
447 shaping the pathophysiology of AD+P. Nevertheless, the precise temporal sequence of these
448 pathological events remains unclear. Our findings lack the resolution to resolve these events as
449 consequences or drivers of disease manifestation. First, our profiling suggests that pre-existing
450 neuropathological changes, namely tau accumulation and glial inflammation, are primary drivers
451 of circuit dynamic changes of upper-layer pyramidal neurons. Notably, both AD-P and AD+P

452 subjects exhibit increased amyloid plaque burden in superficial cortical layers, which may serve
453 as a shared upstream trigger initiating a cascade of neuroinflammatory and neuronal responses.
454 This is congruent with the notion that tau pathology disrupts synaptic integrity[74], which could
455 secondarily enhance transcriptional programs for excitatory drive in an attempt to compensate for
456 declining connectivity. However, it is equally plausible that changes to neuronal activity itself may
457 contribute to synaptic vulnerability and the selective progression of pathology in these circuits. In
458 fact, it has been previously shown that optogenetically increasing neuronal activity can enhance
459 the release and transfer of tau and exacerbate tau pathology[75]. Notwithstanding, our results align
460 with previous findings demonstrating that upper-layer pyramidal neurons exhibit a transitional
461 hyperactive state as a response to amyloid plaques prior to degeneration in AD[76]. Interestingly,
462 this hyperactive state in L2 and L3 pyramidal cells of the prefrontal cortex was similarly marked
463 by the expression of CDK5, SYT1 and SNAP25. This supports the notion that cortical circuits
464 undergo maladaptive compensatory responses, perhaps as an attempt to maintain network
465 integrity in the face of progressive pathology.

466 Secondly, our data suggest that metabolic stress of interneurons may contribute to their
467 dysfunction, further impairing inhibitory tone and perpetuating network dysfunction. Here we
468 reasoned that a potential major consequence of neuronal excitability changes is the increased
469 metabolic burden placed on inhibitory interneurons, which must continuously buffer excessive
470 excitatory input. Alternatively, metabolic impairments in interneurons could be the initiating event,
471 leading to inability to properly regulate excitatory pyramidal neurons and thus driving
472 hyperexcitability and circuit dysfunction. Given that interneurons rely heavily on oxidative
473 metabolism, disruptions in their energy supply potentially mediated by glial inflammation or
474 mitochondrial dysfunction, could precipitate inhibitory failure and circuit instability[77]. Importantly,
475 our findings also implicates microglial exhaustion and senescence in AD+P, which could play a
476 critical role in driving circuit dysfunction. Microglial dysfunction, characterized in AD+P by a loss

477 of homeostatic gene expression and upregulation of stress and senescence markers like
478 CDKN1A (p21), is increasingly recognized as a contributor to impaired neuronal network
479 regulation. While microglial numbers and gross activation markers were unchanged through
480 histology of AD+P postmortem brains, the shift toward an exhausted, inflammatory state suggests
481 loss of microglial functional capacity. Since prior studies have linked microglial loss-of-function to
482 epileptiform activity[78–80], this raises the possibility that microglial senescence in AD+P
483 exacerbates cortical hyperexcitability. This dysfunctional glial state may contribute to the failure
484 of interneurons to maintain inhibitory tone, further amplifying excitatory-inhibitory imbalance and
485 promoting network instability. Understanding the interplay between glial dysfunction, particularly
486 microglial exhaustion, and interneuron vulnerability will be critical for identifying therapeutic
487 strategies that restore network homeostasis in AD+P.

488 Of note, psychosis in dementia has been increasingly linked to dysfunction in the prefrontal cortex
489 (PFC)[81], with our findings highlighting more pronounced transcriptional and cellular alterations in
490 this region compared to the hippocampus. For instance, we found nearly three times more
491 differentially expressed genes in the PFC than in the Hippocampus between AD+P and AD-P.
492 The PFC plays a crucial role in executive function, attention, and reality monitoring, processes
493 that are frequently disrupted in psychotic states, making it a plausible locus for disease-related
494 dysfunction[82]. However, our findings are derived from an aged cohort that spans subjects from 65
495 to 102 years old (average age at death of 86 years old across both groups). Given that the
496 hippocampus is affected earlier in AD[26], it is also possible that by the time of our molecular
497 profiling, the most critical cellular processes contributing to psychosis had already occurred,
498 leaving the PFC as the dominant site of pathology at later disease stages. This raises important
499 questions about whether hippocampal dysfunction in earlier stages plays a fundamental role in
500 initiating psychotic symptoms, with the PFC becoming increasingly impacted as the disease
501 progresses.

502 Our functional studies suggest that the upregulation of CDK5R1, the regulatory subunit of CDK5,
503 may be driven by glial inflammatory responses in AD+P. CDK5 is a key kinase involved in
504 neuronal development and synaptic plasticity, but its dysregulation has also been implicated in
505 tau hyperphosphorylation and neurodegeneration[51]. Notably, inhibition of CDK5 has been shown
506 to ameliorate tau pathology and prevent neuronal loss in preclinical models of AD[83]. Given the
507 strong association between CDK5 activity, tau pathology, and circuit dysfunction in AD+P, our
508 findings suggest that CDK5 inhibitors[84,85] may hold promise for mitigating not only
509 neurodegeneration but also the neuropsychiatric symptoms associated with AD. Future
510 investigations should explore whether CDK5 inhibition can restore synaptic balance and
511 attenuated psychotic symptoms in preclinical AD+P models, paving the way for targeted
512 therapeutic interventions.

513 Additionally, we uncovered convergent and divergent molecular features of psychosis across
514 Alzheimer's disease and schizophrenia by integrating genetic risk and gene expression analysis.
515 Stratified LD score regression revealed that schizophrenia genetic variants were more strongly
516 associated with differentially expressed genes (DEGs) in AD+P than were AD variants,
517 suggesting a shared genetic architecture that may predispose to psychotic symptoms across
518 etiologically distinct disorders. These findings imply that while some neuronal vulnerabilities may
519 be common to psychosis broadly, potentially enabling cross-diagnostic therapeutic strategies,
520 other features are disease-specific and reflect the unique pathophysiological context of AD. As
521 such, treatment development efforts may benefit from a dual approach. For instance, targeting
522 core neuronal stress and synaptic dysregulation pathways shared across AD+P and
523 schizophrenia, while also addressing AD+P-specific mechanisms, such as metabolic vulnerability,
524 to achieve more tailored and effective interventions.

525 Collectively, our findings underscore the need for a deeper mechanistic understanding of the
526 molecular and genetic drivers of psychosis in dementia, an area that remains largely uncharted.

527 As single-cell and multi-omic technologies continue to refine our ability to map disease-associated
528 alterations, the field is poised to leverage this expanding molecular landscape, including datasets
529 like ours, for targeted therapeutic development. A particularly promising avenue is the use of
530 patient-derived iPSCs to model psychosis-associated circuit dysfunction, providing a controlled
531 platform to dissect the genetic contributions to neuronal and glial pathology. However, given the
532 complexity of psychiatric symptoms in dementia and our limited understanding of their genetic
533 underpinnings, these efforts require large-scale iPSC repositories derived from diverse patient
534 cohorts. With greater access to patient genetics, the generation of isogenic lines will allow for
535 more precise manipulation of risk variants, accelerating the discovery of disease-modifying
536 treatments and ultimately guiding the development of more effective therapeutics for psychosis in
537 neurodegenerative disease.

538 ## Methods

539 ### Human postmortem brain samples

540 Postmortem brain tissue samples were obtained from the neuropathology core of the University
541 of Pittsburgh Alzheimer's disease research center. Subjects underwent annual neurological,
542 neuropsychological and psychiatric evaluations as previously described [19,23,86]. An independent
543 committee of experienced clinicians made consensus DSM-IV diagnoses for each subject.
544 Psychosis was defined as the presence of delusions or hallucinations at any visit. Subjects with
545 a pre-existing psychotic disorder (e.g. schizophrenia) were excluded from the study.

546 Brain banking protocols were approved by the local Committee for Oversight of Research and
547 Clinical Training Involving Decedents (CORID). At the time of autopsy, the brain was bisected
548 and the left hemisphere fixed in formalin for subsequent diagnostic evaluation using consensus
549 guidelines [87–90]. The right hemisphere was dissected fresh with multiple aliquots taken from
550 different brain regions and frozen at -80$^{o}$C.

551

552 **Nuclei isolation from frozen postmortem brain tissue for snRNA-seq and snATAC-seq**

553 We extracted nuclei from frozen postmortem brain tissue following an adapted version of the
554 method described by Mathys et al. with some modifications. In brief, brain tissue was
555 homogenized in 700 µL of Homogenization buffer, then filtered through a 40 µm cell strainer
556 (Corning, NY). After adding 450 µL of Working solution, the sample was layered onto a 30%/40%
557 OptiPrep density gradient (750 µL of 30% OptiPrep solution and 300 µL of 40% OptiPrep solution)
558 to form a 25% OptiPrep solution. Nuclei were separated via centrifugation at 10,000g for 5 minutes
559 at 4°C using a fixed rotor tabletop centrifuge. The nuclei pellet was collected from the 30%/40%
560 interphase, transferred to a clean tube, washed twice with 1 mL of ice-cold PBS containing 0.04%
561 BSA (centrifuged at 300g for 3 minutes at 4°C), and resuspended in 100 µL of PBS with 0.04%
562 BSA. After counting, nuclei were diluted to a final concentration of 1000 nuclei per µL.

563 For single-nucleus RNA sequencing (snRNA-seq), the isolated nuclei were processed using the
564 10x Genomics Chromium Single-Cell 3′ Reagent Kits v3, targeting 5000 nuclei per brain region
565 per individual. Library preparation was carried out following the manufacturer's protocol, and
566 sequencing was performed using the Illumina NovaSeq 6000 S2 system (100 cycles). For single-
567 nucleus ATAC sequencing (snATAC-seq), the remaining nuclei were pelleted, resuspended in 1x
568 Diluted Nuclei buffer, and adjusted to a concentration of 2500 nuclei per µL. Library construction
569 was completed using the 10x Genomics Chromium Single-Cell ATAC Reagent Kit v1 according
570 to the manufacturer's instructions, with sequencing conducted on the NovaSeq 6000 S2 platform
571 (100 cycles, Illumina).

572 **snRNA-seq data processing**

573 We processed raw sequencing reads by mapping them to the human reference genome GRCh38
574 and quantified unique molecular identifiers (UMIs) for each gene in each cell using CellRanger
575 v6.1.2 (10x Genomics)[91]. We then pre-processed the resulting gene-cell count matrix using

576 Seurat v4.4.0[92]. For quality control, we retained cells with more than 500 UMIs and less than 5%
577 mitochondrial genes, and included genes expressed in at least 50 cells for further analysis. We
578 normalized UMI counts by total counts per cell, scaled them to 10,000 UMIs per cell, and
579 performed log transformation. We identified the top 2000 highly variable genes for principal
580 component analysis (PCA) and used the top 30 principal components (PCs) to generate a UMAP
581 embedding. To correct for batch effects, we applied Harmony [93]. Clusters were identified using a
582 resolution of 0.5. To filter out potential doublets, we applied DoubletFinder [94] with default
583 parameters and removed cells with a doublet score above 0.2. Additionally, after clustering, we
584 excluded clusters expressing markers from two or more cell types, as they were likely doublets.

585 **snATAC-seq data processing**

586 We processed snATAC-seq data by first generating raw FASTQ files for each sample through
587 demultiplexing with cellranger-atac software(v2.0) [95]. Next, we aligned the reads to the human
588 reference genome (GRCh38) using "cellranger-atac count", producing fragment files for each
589 sample. For downstream analysis, we used ArchR (v1.0.1)[96], removing potential doublets with the
590 "filterDoublets" function. We retained cells with TSS enrichment >6 and fragment counts between
591 1,000 and 100,000 for further analysis. We performed iterative latent semantic indexing (LSI)
592 dimension reduction and clustering using a 500 bp tile-based matrix, setting `iterations=4`,
593 `resolution=0.2`, and `varFeat=50000`. We visualized cell embeddings with UMAP and generated
594 the gene score matrix in ArchR. Cell type annotation was based on gene scores of well-
595 established brain marker genes[97].

596 **Peak calling and differential peak analysis**

597 We identified chromatin accessible peaks using MACS2, following the ArchR pipeline[96,98], and
598 constructed a peak-by-cell matrix. To identify marker peaks for each cell type, we applied a
599 Wilcoxon test in ArchR, using a p-value cutoff of <0.01 and $\log_2$ fold change >0.5. We then
600 annotated the marker peaks with GREAT analysis[99,100] , using the basalPlusExt model and

601 extending 100kb upstream and downstream of each peak. For motif analysis, we expanded peaks
602 to 2000 bp and applied Homer with default parameters [101].

603 **Co-accessibility analysis**

604 We inferred co-accessibility between proximal and distal peaks as a proxy for peak-to-gene links,
605 assessing correlations between peak accessibility and gene expression. We applied the following
606 parameters: corCutOff = 0.3, FDR = 1e-4, upstream = 50,000 bp, downstream = 50,000 bp. The
607 identified peak-gene pairs were further analyzed to link distal accessible peaks with differentially
608 expressed genes in AD with psychosis.

609 **Cell proportional analysis**

610 We performed propeller[102] analysis to evaluate the statistical significance for compositional
611 differences between phenotypic groups with the consideration of the confounding variables in the
612 model including sex, age and TDP pathology. We used the *speckle* package in R and adjusted
613 p-value < 0.05 as cutoff for significance.

614 **Gene Ontology enrichment analysis**

615 We applied Enrichr in R to perform enrichment analysis for Gene Ontology biological process
616 (adjusted p-value < 0.05 as a cutoff)[103,104]. We selected the representative terms for visualization
617 manually based on the diverse functional categories and the number of genes involved in each
618 term.

619 **Immunohistochemistry of postmortem human brains**

620 Formalin-fixed, paraffin-embedded (FFPE) human brain tissue (prefrontal cortex) was sectioned,
621 mounted, and processed at the neuropathology core of the University of Pittsburgh Alzheimer's
622 disease research center (ADRC). Slides were deparaffinized with xylene, and then rehydrated
623 through a series of graded ethanol rinses (e.g., 100%, 95%, 70%) followed by a final rinse with
624 1xPBS before immunostaining. Sections were blocked for 1 h at room temperature (RT) in
625 blocking buffer (PBS containing 5% bovine serum albumin, 1% normal donkey serum and 0.3%

626 Triton X-100). The sections were incubated for 24 hours at 4°C with the primary antibodies in
627 blocking buffer. NeuN (Synaptic Systems; Cat#266 004), Vglut1 (Synaptic Systems; Cat#135
628 302), MAP2 (BioLegend; Cat#822501), Phospho-Tau (Ser202, Thr205)(AT8) (Thermo Fisher
629 Scientific; Cat#MN1020), Phospho-Tau (Ser396) (Thermo Fisher Scientific; Cat#44-752G).
630 Following primary antibody incubation, the sections were washed three times for 5 min each at
631 RT in PBS and then incubated with secondary antibodies (dilution 1:1000) for 2 h at RT. For
632 plaque staining, Methoxy-X04 (Tocris; #4920) was added together with secondary antibodies.
633 The slides were once again washed three times at RT in PBS and incubated in TrueBlack
634 (Biotium; Cat#23007) for 90 seconds. After a final round of washes, the slices were mounted in
635 Fluromount-G (SouthernBiotech; Cat#0100-01). Primary antibodies were visualized with Alexa
636 Fluor 405, Alexa Fluor 488, Alexa Fluor 555, and Alexa Fluor 647 antibodies (Molecular Probes),
637 and cell nuclei visualized with DAPI using a confocal microscope (LSM 900; Zeiss) with a 20× or
638 63× objective. For experiments quantifying fluorescent intensity, images were analyzed with
639 Imaris imaging software (Oxford Instruments).

640 **In situ hybridization with RNAscope in postmortem human brains**

641 Slides of FFPE human brain tissue corresponding to the prefrontal cortex were processed by
642 University of Pittsburgh ADRC and shipped to ACD Biotechne for RNAscope assays and imaging.
643 Brain sections were probed for human SYN1, STAT3, and GFAP and counterstained with DAPI.
644 Slides were imaged with a slide scanner and files shared from ACD Biotechne were quantified
645 with Slideviewer software from 3D Histech.

646 **Gene overexpression, plasmid cloning, lentivirus production**

647 We obtained AAV-hsyn-CheRiff-eGFP from Adam Cohen through Addgene (Plasmid #51697),
648 then subcloned it into a lentiviral vector carrying a second promoter PGK driving blasticidin
649 resistance cassette (Addgene; #666808) to create a lentiviral construct that would allow for the
650 generation of a stable cell line expressing neuronal-restrictived hSyn-CheRiff upon transduction

651 and selection with blasticidin in iPSCs prior to organoid derivation. After antibiotic selection,
652 colonies were confirmed to carry hSyn-CheRiff via PCR screening. For overexpression screen in
653 organoids, we populated a list of 51 up-regulated DEGs from L2/L3 from the following GO terms:
654 neuron projection morphogenesis (GO:0048812), regulation of neuron projection development
655 (GO:0010975), positive regulation of neuron projection development (GO:0010976), neuron
656 projection development (GO:0031175), and neuron projection organization (GO:0106027). Of
657 these, 37 were commercially available in lentiviral vectors through the plasmid repository at
658 DNASU (Arizona State University, dnasu.org). Received plasmids were made into lentivirus using
659 established protocols and as reported in Victor et al., Cell Stem Cell 2022. Organoids were
660 transduced separately with each virus or a control construct under the same conditions carrying
661 the mammalian codon optimized variant of the blue fluorescent protein, azurite (pLv-Azurite;
662 Addgene #36086).

663 **iPSC Cultures, Generation of Forebrain Organoids, and Assembloids**

664 Human iPSC line used in this study was derived from a healthy donor (APOE3/3 genotype) and
665 generated by the Picower Institute for Learning and Memory iPSC Facility as first described (Lin
666 et al., 2018). iPSCs were maintained at 37°C and 5% CO2, in feeder-free conditions in mTeSR1
667 medium (Cat #85850; STEMCELL Technologies) on Matrigel-coated plates (Cat # 354277;
668 Corning; hESC-Qualified Matrix). iPSCs were passaged at 60–80% confluence using ReLeSR
669 (Cat# 05872; STEMCELL Technologies) and reseeded 1:6 onto Matrigel-coated plates. Dorsal
670 forebrain organoids were generated using a previously established protocol (Sloan et al., 2018)
671 with an adapted iPS seeding strategy (Marton et al., 2019), as described previously in Victor et
672 al., Cell Stem Cell 2022. After 60 days of culture, organoids were transduced with lentivirus or
673 AAVs and cultured separately for an additional 2 weeks. Next, pairs of organoids with desired
674 infected constructs were moved to microcentrifuge tubes and allowed to fuse for 24 hours to
675 generate assembloids. Following fusion, assembloids were cultured separately in untreated glass

676 bottom 24-well microplates (Cat #82421; Ibidi) and fed every 3-4 days with experiments starting
677 approximately at 90 days in vitro.
678
679 **Calcium Reporter, Imaging, and Optogenetic Stimulation**
680 Organoids were infected with pAAV.Syn.GCaMP6s.WPRE.SV40 (Cat#100843-AAV1; Addgene)
681 while temporarily plated in 24-well plates (3-4 organoids per well) with 20ul of viral prep (100 µL
682 at titer ≥ $1\times10^{13}$ vg/mL). After overnight incubation with virus, organoids were returned to ultra-low
683 attachment 10cm dishes. Typically within 12-14 days calcium dynamics were easily detectable.
684 For experiments with AAV Axonal GCaMP6s, a similar protocol was followed but with pAAV-
685 hSynapsin1-axon-GCaMP6s (Plasmid #111262). For calcium imaging, live-imaging was
686 performed with Zeiss LSM900 equipped with a heated chamber kept at 37 C with humidity and
687 CO2 control. Images were processed and analyzed as described previously (Victor et al., Cell
688 Stem Cell 2022). Calcium traces from motion-corrected time series were manually segmented on
689 ImageJ into individual cells based on threshold intensity, variance, and upper and lower limits for
690 cell size. Image segmentation results were separately inspected for quality control. Fluorescence
691 signal time series (DF/F: change in fluorescence divided by baseline fluorescence) were
692 calculated for each segment. The baseline fluorescence for each cell was determined as the
693 minimum fluorescence signal in the baseline recording epoch. For GCaMP-tagged neurons, The
694 onset of a calcium transient occurred when DF/F exceeded two standard deviations above the
695 baseline fluorescence. The termination of a calcium transient was identified as occurring when
696 DF/F fell below 0.5 standard deviations above the baseline fluorescence. We defined a
697 multicellular ensemble events when the number of simultaneously active cells exceeded 60% of
698 all cells. For CheRiff-GCaMP6s assembloid screen, optogenetic stimulation and calcium imaging
699 were coupled and acquired using low magnification 2.5x objective to scan the entire assembloid
700 structure. For experiments with chronic optogenetic stimulation, custom LED tissue culture plates

701 were outfitted under the control of an Arduino board and stimulation carried out for 200ms at 10Hz
702 every 2 minutes for 48 hours. Heatmaps were generated using GraphPad Prism (GraphPad
703 Software).

704 **Patch-Clamp Electrophysiology**

705 Whole-cell patch-clamp recordings of neurons were performed at 6 to 8 weeks after NGN2
706 induction from hSyn-CheRiff iPSC line. Intracellular recordings were performed at room
707 temperature using an Axon CV-7B headstage, Multiclamp 700B amplifier, and Digidata 1440A
708 digitizer (Molecular Devices). Electrode pipettes were pulled from borosilicate glass on a Model
709 P-97 Flaming/Brown micropipette puller (Sutter Instrument) and ranged between 4–7 MΩ
710 resistance. Intrinsic neuronal properties were studied using the following solutions (in mM):
711 Extracellular: 125 NaCl, 2.5 KCl, 1.2 NaH2PO42H2O, 1.2 MgCl26H2O, 2.4 CaCl22H2O, 26
712 NaHCO3, 11 glucose (pH 7.4). Intracellular: 135 K-gluconate, 5 KCl, 2 MgCl26H2O, 10 HEPES,
713 2 Mg-ATP, 0.2 Na2GTP (pH 7.2). Membrane potentials were typically kept at -70 mV. In current-
714 clamp mode, action potentials were elicited by photostimulation with blue light. Data was first
715 collected and analyzed using pCLAMP 11 software (Molecular Devices).

716 **MEA Recordings**

717 Intact organoids were plated onto Poly-D-Lysine (Cat#P6407-10X5MG; Sigma-Aldrich) coated
718 wells of a CytoView MEA 48-well plate (Cat#M768-tMEA-48B; Axion BioSystems) and covered in
719 a Matrigel droplet (Cat # 354277; Corning) to anchor the organoid. After 15–30 min in 37 C,
720 droplets were flooded with warm BrainPhys Medium (Cat#05790; STEMCELL Technologies) and
721 allowed to recover for at least four weeks before recording sessions. A recording session
722 preceded the 5ng/ml IL-6 treatment, denoted as baseline recording. For optogenetic stimulation,
723 organoids were pulsed continuously at 6Hz with blue light. All extracellular recordings were
724 performed using the Axion Maestro Pro MEA system (Axion Biosystems). Spontaneous neural
725 activity was recorded for 15 min at a sampling rate of 12.5 kHz, and an adaptive threshold set at

726 5.5 times the standard deviation of baseline noise was used for spike detection. Electrodes were
727 defined as active if neuronal firing occurred at a minimal rate of 5 spikes/min. For MEA data
728 analysis, only wells containing a minimum of 3 active electrodes were included. Neuronal firing
729 metrics were exported as the averages from each well from Axion Biosystems' Neural Metrics
730 Tool and plotted with Prism GraphPad (GraphPad Software). For optogenetic stimulation, custom
731 blue LED panels were adapted to fit the Axion Maestro Pro and delivered under the control of an
732 Arduino board at 6Hz.

733 **Gene Expression analysis with qPCR**

734 RNA extraction for qPCR analysis was performed with RNeasy Plus Mini Kit (Cat# Cat#74134;
735 Qiagen), and reverse transcription was performed with RNA to cDNA EcoDry Premix (Cat#
736 Cat#639549; Takara) according to the manufacturer's instructions. Gene expression was
737 analyzed with Real-Time PCR (CFX96; Bio-Rad) and SsoFast EvaGreen Supermix
738 (Cat#1725202; Bio-Rad). Expression data was normalized to house-keeping gene GAPDH using
739 the 2 DDCT relative quantification method. CDK5R1 expression was assessed with primers (5' -
740 > 3'): Forward - AGAACAGCAAGAACGCCAAG and Reverse - CGGCCACGATTCTCTTCCA.
741 Housekeeping primers for GAPDH (5' -> 3'): Forward - AGAAGGCTGGGGCTCATTTG and
742 Reverse - AGGGGCCATCCACAGTCTTC.

743 **Identification of differentially expressed genes between AD with and without psychosis**

744 We applied two methods (one single-cell based method, MAST, and a single-cell based method
745 edgeR) to detect the differentially expressed genes for each cell type between AD with and without
746 psychosis individuals per brain region. We controlled the covariates for both methods, including
747 percentage of mitochondrial genes, percentage of ribosomal genes, age, sex, PMI, and TDP
748 pathology. The genes with FDR <= 0.05 for MAST and p-value <= 0.05 for edgeR were selected
749 for further analysis. We found the DEGs were highly consistent between two methods.

750 **Prediction of upstream transcription factors**

751 We inferred the upstream transcription factors of genes (marker genes or DEGs) using Enrichr in
752 R for the enrichment-based analysis based on three libraries including TRANSFAC and JASPAR,
753 ChEA, and ENCODE TF ChIP-seq data [66,105,106]. We used adjusted p-value <0.05 as a cut-off to
754 select the significant TFs. For motif-based analysis, we linked the DEGs to distal peaks using the
755 peak-to-gene links represented by co-accessible peaks and then performed motif analysis by
756 expanding the peaks to 2000bp with the default parameters in Homer [101]. We kept the TFs with
757 detected expression (average expression > 1 after log2 transformation) in relevant cell types for
758 further analysis.

759 **LDSC Heritability Enrichment Analysis**

760 We applied Stratified Linkage Disequilibrium Score Regression (S-LDSC)[73] to evaluate the
761 heritability enrichment of genetic risk for Schizophrenia and AD within DEGs related accessible
762 chromatin regions. To focus on functionally relevant elements, we first identified distal accessible
763 peaks linked to DEGs in AD+P individuals by leveraging co-accessibility between promoter and
764 distal regulatory regions. For these DEG-linked peaks, we generated binary annotation files
765 indicating whether each SNP overlapped with an accessible region. To account for genetic
766 variants in linkage disequilibrium (LD) and address the sparsity of variant annotations, we
767 extended annotated regions by 1000 bp to both directions. We formatted these annotations
768 according to the standard S-LDSC pipeline and computed LD scores using the 1000 Genomes
769 Project Phase 3 European reference panel. We then estimated partitioned heritability with publicly
770 available Schizophrenia and AD GWAS summary statistics[107,108], which include SNP-level effect
771 sizes and standard errors. We defined enrichment as the proportion of heritability explained by
772 SNPs within accessible peaks relative to the proportion of SNPs in those peaks. A significant
773 enrichment suggests that disease-associated variants are preferentially located within regulatory
774 elements specific to the cell types under investigation.

775 **Figure Legend**

776 **Figure 1. snRNA-seq atlas of PFC and hippocampus from AD patients with psychosis. A.**
777 Experimental design and UMAPs of 160,875 nuclei with annotated cell types in snRNA-seq data.
778 The three UMAPs on the left show the high-resolution of cell types in excitatory neurons, inhibitory
779 neurons and vasculature. **B.** Dotplot shows the expression of well-known marker genes for major
780 cell types in the human brain. The color represents the expression level and the size of the dot
781 represents the percentage of cells with expression. **C.** Cell fraction distribution of major cell types
782 in AD w/wo psychosis. Propeller analysis to determine the statistical significance highlighted with
783 *. **D.** Cell fraction distribution of excitatory neuron subtypes in AD w/wo psychosis. Propeller
784 analysis to determine the statistical significance highlighted with *, (n= 24 AD-P and 24 AD+P;
785 see Table S1 for patient manifest). **E.** Immunostaining for the neuronal marker NeuN, stratified
786 by cortical layer based on nuclear density of DAPI (n= 10 AD-P and 10 AD+P). Two-Way ANOVA
787 with Bonferroni post-hoc test. ns= not significant, *p-value <0.05. **F.** Immunostaining for the
788 excitatory neuronal marker VGLUT1 as counterstain for the amyloid plaque stain, Methoxy-X04.
789 Plaque density mapped across cortical layers (n=20 AD-P and AD+P combined). No overall
790 significant difference in PFC, but near-significant trend for increased plaques in layer L4 based
791 on Two-Way ANOVA with Bonferroni post-hoc test; plotted separately for panel only. **G.**
792 Immunostaining for MAP2, Methoxy-X04 and phospho-tau (pTau, AT8). pTau density across
793 cortical layers for AD-P and AD+P. **H.** Overall increase in pTau density in PFC (n= 10 AD-P and
794 10 AD+P); Student's t-test, *p-value <0.05.

795 **Figure 2. Cell-type-specific and brain-region-specific transcriptional changes in AD with**
796 **psychosis. A.** Heamaps show the log fold change of up-regulated and down-regulated genes
797 per cell type in prefrontal cortex (SF). The top 5 DEGs per cell type are highlighted on the right
798 side of the heatmap. **B.** Heamaps show the log fold change of up-regulated and down-regulated
799 genes per cell type in hippocampus (AH). The top 5 DEGs per cell type are highlighted on the
800 right side of the heatmap. **C.** The comparison of DEGs in AD+P between AH and SF per major

801 cell type. Six groups of genes represent up-regulated and down-regulation sharing by two regions
802 or unique to one region. For each heatmap, the left half shows whether the DEGs are significant
803 (1 or 0) and the right half shows the real log fold change to present whether the change suggests
804 the same direction between two regions. **D.** Significantly enriched and representative Gene
805 Ontology (GO) terms in excitatory neurons binned in six groups based on shared or unique
806 expression across brain tissue.

807 **Figure 3. Upregulation of Synaptic-Related Genes is a Compensatory Mechanism Evoked**
808 **by Surviving Excitatory Neurons. A.** Heatmap of DEGs in GO terms related to synaptic
809 transmission, neurotransmitter signaling, neuronal development and neuronal projection
810 morphogenesis across cortical layers. **B.** Histology of PFC human brain sections with H&E
811 (hematoxylin and eosin) staining and fluorescent in situ RNA hybridization using an RNAscope
812 probe for synapsin 1 (SYN1) from AD+P (n=3) and AD-P (n=3) subjects. **C.** Quantification of
813 RNAscope dots per nucleus for a given SYN1-positive neuron (comprising at least 3 SYN1 dots)
814 increased in AD+P across cortical layers. *p-value <0.05, multiple t-tests adjusted for false
815 discovery rate. And in Layers L2/L3. **D.** Higher magnification insets of layers L1, L2 and L3 with
816 SYN1 probe in green and DAPI in blue. **E.** Percentage of cells SYN1-positive ( at least 3 SYN1
817 dots) in cortical layers L2 and L3 were significantly reduced in AD+P. (n=averages of 3 subjects
818 per group). *p-value <0.05, **p-value <0.01, Student's t-test. **F.** Cell fraction analysis from PFC
819 snRNA-seq of inhibitory interneurons. n= 24 subjects per group of snRNA-seq. Propeller analysis
820 to determine statistical significance. **G.** Top GO terms from AD+P DEGs of Parvalbumin (PV)-
821 positive cells.

822 **Figure 4. Functional Characterization of AD+P DEGs from Upper-Layers Excitatory**
823 **Neurons in iPSC-derived Brain Organoids. A.** Outer surface of an organoid derived from an
824 iPSC line that constitutively expresses the channelrhodopsin variant CheRiff under the neuronal-
825 restrictive promoter human Synapsin (hSyn-CheRiff). **B.** Whole-cell patch-clamp

826 electrophysiology of iPSC-derived neurons harboring hSyn-CheRiff paced at 5Hz and 10Hz with
827 blue light stimulation. **C.** AAV Axonal GCaMP6s infected organoids were fused with non-infected
828 organoids to generate assembloids. Neuronal activity was assessed via calcium-imaging at the
829 assembloid junction line, and calcium traces are shown for axonal spikes as the change in
830 fluorescence over baseline fluorescence (ΔF/F). **D.** Assembloid input-output connectivity model
831 with optogenetic stimulation to drive neuronal activity in one hemisphere and calcium imaging to
832 readout for neuronal activity in the other hemisphere. **E.** Live-imaging of assembloids showing
833 high-amplitude calcium events in the contralateral organoid. Color gradient represents minimum
834 (purple) and maximum (yellow) levels of calcium amplitude. **F.** Rasterplot showing highly
835 coordinated ensemble calcium activity dynamics. Change in fluorescence shown as Delta F/F. **G.**
836 Assembloid quantification of contralateral calcium dynamics in response to optogenetic
837 stimulation to the ipsilateral organoid overexpressing 37 genes from up-regulated DEGs in AD+P
838 pyramidal upper-cortical layer neurons (L2 and L3) from snRNA-seq data. Data was ranked and
839 binned into 3 groups (increased activity, no change, or reduced activity) based on Two-Way
840 ANOVA with Bonferroni post-hoc test results. Calcium traces from the time series were manually
841 segmented on ImageJ into individual cells based on threshold intensity results in n=15-88
842 neuropils per organoid and plotted for maximum amplitude. Control assembloids were transduced
843 with a lentiviral vector encoding the blue fluorescent protein EBFP. **H**. Quantification of EGFP
844 intensity on the contralateral organoid that traversed the assembloid junction line from hSyn-
845 CheRiff ipsilateral organoid ranked from least to most fluorescent intensity. **I**. Representative
846 image of hSyn-CheRiff across junction line from control and CDK5R1 overexpressing assembloid.
847 **J.** Calcium dynamics in organoids 14 days post infection with CDK5R1 or EBFP lentivirus.
848 Student's t-test, *p-value <0.05, n= 5 organoids per group. **K**. Quantification of phospho-Tau
849 (pTau) fluorescence levels in organoids infected with CDK5R1 or EBFP controls. Student's t-test,
850 **p-value <0.01, n= 3 organoids per group. **L**. Immunohistochemistry in postmortem brains
851 showing increased CDK5R1 fluorescent intensity in PFC (n= 10 AD-P and 10 AD+P); Student's

852 t-test, *p-value <0.05.

853 **Figure 5. Glial Response in AD+P PFC is Marked by Microglial Exhaustion and Astrocyte-**
854 **Driven Inflammation. A.** Representative GO terms for microglia and astrocytes from PFC DEGs.
855 **B.** Histology for microglia-marker P2RY12 in PFC. Student's t-test, ns= not significant, n= 10 AD-
856 P and 10 AD+P. **C.** Volcano plot for up and down-regulated genes in AD+P PFC microglia. **D.**
857 Immunofluorescence with the atrocyte-marker GFAP quantified across PFC cortical layers and
858 white matter (wm) normalized per area. Student's t-test, ns= not significant, n= 10 AD-P and 10
859 AD+P postmortem brains. **E.** GFAP quantification binned by cortical layers. Two-Way ANOVA
860 with Bonferroni post-hoc test. ns= not significant, **p-value <0.01, n= 10 AD-P and 10 AD+P
861 postmortem brains. **F.** Transcriptional Regulatory Network (TRN) from astrocyte top GO term
862 "cellular response to cytokine stimulus". **G**. RNAscope for STAT3 and GFAP. (n= 3 AD-P and 4
863 AD+P); Student's t-test, *p-value <0.05. H. Ranked Pathway Interaction Database (PID)
864 Pathways. **I.** hSyn-CheRiff organoid seeded on multielectrode array (MEA) and raw traces from
865 recordings of the same organoid at baseline and after 5 ng/ml of IL-6. **J.** Paired t-test, n= 7
866 organoids recorded at baseline and again following overnight incubation with IL-6, *p-value <0.05.
867 **K.** qPCR for CDK5R1 following treatment of 5 ng/ml of IL-6. (n= 4 organoids per group); Student's
868 t-test, **p-value <0.01.

869 **Figure 6. Epigenetic regulation of cell-type-specific gene expression changes and their**
870 **association with genetics. A-C.** UMAPs of 241,430 nuclei in snATAC-seq data with annotated
871 cell types (**A**), brain regions (**B**) and pathological groups (**C**). **D.** GREAT enrichment analysis for
872 cell type specific peaks to show the function relevance with certain cell types. The color represents
873 the log2 fold change and the size of dots represents the significance. **E**. The diagram to show the
874 co-accessible gene-peak pairs and their applications in TF identification and genetic association
875 analysis by LDSC. TF enrichment for up-regulated DEGs and down-regulated DEGs per cell type.
876 The dotplot shows the motif enrichment significance by color and TF-target enrichment

877 significance by size of dots. **F.** AD+P DEGs linked chromatin accessible peaks show the
878 heritability enrichment of genetic variants implicated for Schizophrenia using S-LDSC analysis.
879 The barplot shows the enrichment score, where pink ones represent nominally significant cell
880 types. The -log10 of p-value is shown by the blue point. The red dash line represents the stringent
881 threshold with p-value < 0.01.**G**. Representative Gene Ontology terms enriched in AD+P unique
882 down-regulated DEGs. **H**. Representative Gene Ontology terms enriched in AD+P unique up-
883 regulated DEGs. **I**. The UpSet plot shows the overlap of DEGs between Alzheimer's Disease
884 (AD), Schizophrenia (Sz) and AD+P (ADP). The pink bars show the significant intersections. The
885 blue and red bars show the AD+P specific down-/up-regulated DEGs.
886

887 ## Supplementary Figure Legend

888 **Figure S1. Histology for Neuropathological Changes in AD-P and AD+P.** An additional cohort
889 of postmortem human brain tissue from 20 subjects (n= 10 AD-P and 10 AD+P). Error bar
890 represents the SEM. Two-way ANOVA with Bonferroni's multiple comparison test.

891 **Figure S2. Cell Fraction Analysis for Anterior Hippocampus in AD-P and AD+P.** Propeller
892 analysis was used to determine statistical significance. Error bar represents the SEM. ns= not
893 significant. n= 24 AD+P and 24 AD-P postmortem human brain tissue. AH: Anterior Hippocampus.

894 **Figure S3.Transcriptional Changes in AD with Psychosis. A-B.** Scatter plot to show the
895 consistency of transcriptional changes identified by two methods in SF (**A**) and AH (**B**). The X-
896 axis represents the coefficient calculated by MAST, while the Y-axis represents the log
897 transformed fold change calculated by edgeR.

898 **Figure S4. Gene Ontology (GO) for Transcriptional changes in AD with psychosis.**
899 Representative Gene Ontology from significantly enriched terms for five cell types.

900 **Figure S5. GO Terms from PFC DEGs in Excitatory and Inhibitory Neuronal Subtypes.** Top

901 10 terms for excitatory neurons catalogued by layer (L2/L3, L4 and L5) and inhibitory neurons
902 catalogued by cell type (VIP+, PV+ or SST+ interneurons).

903 **Figure S6. CAMK2B Overexpression Renders Forebrain Organoids Vulnerable to**
904 **Excitotoxicity. A.** Custom LED Tissue Culture Plate. **B-C**. Diagram of experimental design **D**.
905 Stimulation protocol. **E**. Control organoids were tagged with pLenti CMV-EBFP. **F**. Organoids
906 tagged with AAV hSYN-RFP before (baseline) and after stimulation (post-stim) and quantified
907 (**G**). Paired t-test; **p-value<0.01, ns= not significant. n=10 control and 10 CAMK2B
908 overpressing organoids).

909

910 **Figure S7. Epigenetic Regulation of Cell-type-specific Gene Expression Changes. A.**
911 Dotplot shows the gene activity score of well-known marker genes for major cell types in the
912 human brain in snATAC-seq data. The color represents the activity level and the size of the dot
913 represents the percentage of cells with activity. **B**. The composition of major cell types in snATAC-
914 seq data in two brain regions, AH and SF. **C.** The comparison of cell fractions captured by
915 snATAC-seq and snRNA-seq data in two brain regions. **D-E**. UMAPs to show the integrative
916 analysis of snATAC-seq and snRNA-seq data in two brain regions. The UMAP on the left
917 represents the joint map, and the right panel represents the nuclei from single modality. The nuclei
918 were colored by major cell types. **F.** The number of peaks per cell type and union set, colored by
919 their genomic locations (distal, exonic, intronic or promoter regions). **G**. The heamap to show the
920 links between distal peak to promoter peaks, representing the co-accessbility between distal
921 enhancer and promoter. Each row represents one link and each column represents randomly
922 selected nuclei (500 in total for visualization). The left panel represents the activity in snATAC-
923 seq, and the right plan represents the gene expression. Z-score values were used. Most of the
924 links were cell-type specific.

925 **Figure S8. Cell-type-specific Gene Expression Changes and their Association with**

926 **Schizophrenia Genetics. H.** AD+P DEGs linked chromatin accessible peaks show the less
927 enrichment of genetic variants of AD using LDSC analysis. The barplot shows the enrichment
928 score, where pink ones represent the significance. The -log10 of p-value is shown by the blue
929 point. The red dash line represents the stringent threshold with p-value < 0.01. **I-J**. The UpSet
930 plot shows the overlap of DEGs in inhibitory neurons (**I**) and glial cell types (**J**) between
931 Alzheimer's Disease (AD), Schizophrenia (Sz) and AD+P (ADP).

932 ## Supplementary Tables and Movies

933

934 **Table S1. Patient Manifest for snRNA-seq and snATAC-seq.**

935 **Table S2. Patient Manifest for Histology Experiments.**

936 **Table S3. Prefrontal Cortex (PFC) DEGs.**

937 **Table S4. Anterior Hippocampus (AH) DEGs.**

938 **Table S5. PFC Neuronal GO Terms.**

939 **Table S6. PFC Non-Neuronal GO Terms.**

940 **Table S7. GREAT Analysis.**

941 **Table S8. Peak-to-Gene Links.**

942 **Movie S1. Axonal GCaMP at Assembloid Junction Line.**

943 **Movie S2. Representative CheRiff-GCaMP Assembloid.**

944 **Movie S3. Functional Screen for L2/L3 DEGs on Assembloids**

945 ## Acknowledgements

946 We thank the study participants and staff of the Alzheimer Disease Research Center at the

University of Pittsburgh and the brain banking teams and histology staff of the neurodegenerative brain bank at the University of Pittsburgh. The Tsai lab research was made possible through the generous support of the Robert A. and Renee E. Belfer Family Foundation, The Freedom Together Foundation, Eduardo Eurnekian, Lester A. Gimpelson, the Donald A. Mattes (1967) Memorial Neuroscience Research Expendable Fund and Glenda G. Mattes and Steve Corbin, David Emmes, the J. Crayton Pruitt Foundation, and Joseph P. DiSabato and Nancy E. Sakamoto. This work was also supported in part by NIH grants: R01AG062335 (M.K. and L.-H.T.), R01AG081017 (M.K.), R01MH109978 (M.K.), U01MH119509 (M.K.), R01AG074003 (M.K. and L.-H.T.), U01NS110453 (M.K. and L.-H.T.), R01AG058002 (M.K. and L.-H.T.), RF1AG062377 (L.-H.T.), RF1AG054012 (L.-H.T. and M.K.), R01AG067151 (M.K.), UH3NS115064 (L.-H.T. and M.K.), RF1NS129032 (M.K.), R01NS127187 (M.K.), U01AG077227 (L.-H.T.), U01HG012009 (M.K.), U01DA053631 (M.K.), R01DA054584 (M.K.), R01HG008155 (M.K.), H116046 (J.K.K., and R.A.S.), P30-AG066468 (J.K.K., and R.A.S.) and grants from the Cure Alzheimer's Fund CIRCUITS consortium (M.K. and L.-H.T), The Biswas Family Foundation and the Milken Institute (M.K.), and the Alana Foundation (M.K.). M.B.V. is supported by the Howard Hughes Medical Institute Hanna H. Gray Fellowship.

## Data and code availability

The dataset generated in this study will be made publicly available upon publication. Additional supporting datasets are available from the corresponding author upon reasonable request. All code used for data processing and analysis will be released at https://github.com/nasunmit/ at the time of publication.

## Author contributions

M.B.V, N.S., R.A.S., L.-H.T., and M.K. conceived and designed the study; R.A.S., M.K. and L.-

971 H.T. supervised the study; J.K.K. supervised histological experiments, guided data interpretation,
972 and collaborated in study design; N.S. developed the computational framework and conducted
973 data analysis with assistance from Y.T.; M.B.V., N.L., A.N.S., and S.P. performed in vitro
974 experiments and analyzed results; K.G., H.M., X.J., L.-L.H. and A.P.N. performed snRNA-seq
975 and snATAC-seq profiling; L.L. performed electrophysiology analysis; N.S., J.K.K. and M.B.V
976 wrote methods; R.A.S. and J.K.K. provided postmortem samples and scientific input; and M.B.V,
977 N.S., R.A.S., L.-H.T. and M.K. wrote and revised the manuscript.

978

979 ## References


980 1. Lively, S. T. *Activities of Daily Living (ADL): Cultural Differences, Impacts of Disease and*
981 *Long-Term Health Effects*. (Nova Science Publishers, 2015).
982 2. The spectrum of behavioral changes in Alzheimer's disease. *Neurology*
983 https://www.neurology.org/doi/10.1212/WNL.46.1.130.
984 3. Knopman, D. S. *et al.* Alzheimer disease. *Nature Reviews Disease Primers* **7**, 1–21 (2021).
985 4. Schuff, N. *et al.* MRI of hippocampal volume loss in early Alzheimer's disease in relation to
986 ApoE genotype and biomarkers. *Brain* **132**, 1067–1077 (2009).
987 5. Salat, D. H., Kaye, J. A. & Janowsky, J. S. Prefrontal gray and white matter volumes in
988 healthy aging and Alzheimer disease. *Arch Neurol* **56**, 338–344 (1999).
989 6. Canter, R. G., Penney, J. & Tsai, L.-H. The road to restoring neural circuits for the
990 treatment of Alzheimer's disease. *Nature* **539**, 187–196 (2016).
991 7. Xu Lou, I., Chen, J., Ali, K., Shaikh, A. L. & Chen, Q. Mapping new pharmacological
992 interventions for cognitive function in Alzheimer's disease: a systematic review of
993 randomized clinical trials. *Front Pharmacol* **14**, 1190604 (2023).
994 8. Murray, P. S., Kumar, S., Demichele-Sweet, M. A. A. & Sweet, R. A. Psychosis in
995 Alzheimer's disease. *Biol Psychiatry* **75**, 542–552 (2014).

9. Ismail, Z. *et al.* Psychosis in Alzheimer disease - mechanisms, genetics and therapeutic opportunities. *Nat Rev Neurol* **18**, 131–144 (2022).
10. American Psychiatric Association. *The American Psychiatric Association Practice Guideline on the Use of Antipsychotics to Treat Agitation or Psychosis in Patients With Dementia*. (American Psychiatric Pub, 2016).
11. Narang, P. *et al.* Antipsychotic drugs: sudden cardiac death among elderly patients. *Psychiatry (Edgmont)* **7**, 25–29 (2010).
12. Schneider, L. S. & Dagerman, K. S. Psychosis of Alzheimer's disease: clinical characteristics and history. *J Psychiatr Res* **38**, 105–111 (2004).
13. DeMichele-Sweet, M. A. A. *et al.* Genome-wide association identifies the first risk loci for psychosis in Alzheimer disease. *Mol Psychiatry* **26**, 5797–5811 (2021).
14. DeMichele-Sweet, M. A. A. *et al.* Genetic risk for schizophrenia and psychosis in Alzheimer disease. *Mol Psychiatry* **23**, 963–972 (2018).
15. Shah, C., DeMichele-Sweet, M. A. A. & Sweet, R. A. Genetics of psychosis of Alzheimer disease. *Am J Med Genet B Neuropsychiatr Genet* **174**, 27–35 (2017).
16. Antonsdottir, I. M. *et al.* Genetic associations with psychosis and affective disturbance in Alzheimer's disease. *Alzheimers Dement (N Y)* **10**, e12472 (2024).
17. Jauhar, S. *et al.* The relationship between cortical glutamate and striatal dopamine in first-episode psychosis: a cross-sectional multimodal PET and magnetic resonance spectroscopy imaging study. *Lancet Psychiatry* **5**, 816–823 (2018).
18. Basavaraju, R. *et al.* Hippocampal Glutamate and Positive Symptom Severity in Clinical High Risk for Psychosis. *JAMA Psychiatry* **79**, 178–179 (2022).
19. DeChellis-Marks, M. R. *et al.* Psychosis in Alzheimer's Disease Is Associated With Increased Excitatory Neuron Vulnerability and Post-transcriptional Mechanisms Altering Synaptic Protein Levels. *Front Neurol* **13**, 778419 (2022).
20. Kouhsar, M. *et al.* A brain DNA co-methylation network analysis of psychosis in Alzheimer's

1022 disease. *Alzheimers Dement* **21**, e14501 (2025).
1023 21. Rikandi, E. *et al.* Functional network connectivity and topology during naturalistic stimulus is
1024 altered in first-episode psychosis. *Schizophr Res* **241**, 83–91 (2022).
1025 22. Song, X. *et al.* Bioenergetics and abnormal functional connectivity in psychotic disorders.
1026 *Mol Psychiatry* **26**, 2483–2492 (2021).
1027 23. Murray, P. S. *et al.* Hyperphosphorylated tau is elevated in Alzheimer's disease with
1028 psychosis. *J Alzheimers Dis* **39**, 759–773 (2014).
1029 24. Almeida, F. C. *et al.* Psychosis in Alzheimer's disease is associated with specific changes
1030 in brain MRI volume, cognition and neuropathology. *Neurobiol Aging* **138**, 10–18 (2024).
1031 25. Gomar, J. J. *et al.* Increased retention of tau PET ligand [F]-AV1451 in Alzheimer's Disease
1032 Psychosis. *Transl Psychiatry* **12**, 82 (2022).
1033 26. DeTure, M. A. & Dickson, D. W. The neuropathological diagnosis of Alzheimer's disease.
1034 *Molecular Neurodegeneration* **14**, 1–18 (2019).
1035 27. Hedegaard, C. *et al.* Porcine synapsin 1: SYN1 gene analysis and functional
1036 characterization of the promoter. *FEBS Open Bio* **3**, 411–420 (2013).
1037 28. Pickel, V. M. & Segal, M. *The Synapse: Structure and Function*. (Elsevier, 2013).
1038 29. Zhang, Z. & Sun, Q.-Q. The balance between excitation and inhibition and functional
1039 sensory processing in the somatosensory cortex. *Int Rev Neurobiol* **97**, 305–333 (2011).
1040 30. Liu, Y. *et al.* A Selective Review of the Excitatory-Inhibitory Imbalance in Schizophrenia:
1041 Underlying Biology, Genetics, Microcircuits, and Symptoms. *Front Cell Dev Biol* **9**, 664535
1042 (2021).
1043 31. Beasley, C. L. & Reynolds, G. P. Parvalbumin-immunoreactive neurons are reduced in the
1044 prefrontal cortex of schizophrenics. *Schizophr Res* **24**, 349–355 (1997).
1045 32. Beasley, C. L., Zhang, Z. J., Patten, I. & Reynolds, G. P. Selective deficits in prefrontal
1046 cortical GABAergic neurons in schizophrenia defined by the presence of calcium-binding
1047 proteins. *Biol Psychiatry* **52**, 708–715 (2002).

1048 33. Bitanihirwe, B. K. Y. & Woo, T.-U. W. Transcriptional dysregulation of γ-aminobutyric acid
1049 transporter in parvalbumin-containing inhibitory neurons in the prefrontal cortex in
1050 schizophrenia. *Psychiatry Res* **220**, 1155–1159 (2014).
1051 34. Agetsuma, M., Hamm, J. P., Tao, K., Fujisawa, S. & Yuste, R. Parvalbumin-Positive
1052 Interneurons Regulate Neuronal Ensembles in Visual Cortex. *Cereb Cortex* **28**, 1831–1845
1053 (2018).
1054 35. Hu, H., Gan, J. & Jonas, P. Interneurons. Fast-spiking, parvalbumin$^{+}$ GABAergic
1055 interneurons: from cellular design to microcircuit function. *Science* **345**, 1255263 (2014).
1056 36. Hensch, T. K. & Fagiolini, M. *Excitatory-Inhibitory Balance: Synapses, Circuits, Systems*.
1057 (Springer Science & Business Media, 2012).
1058 37. Singer, W., Sejnowski, T. J. & Rakic, P. *The Neocortex*. (MIT Press, 2019).
1059 38. Gerfen, C. R., Economo, M. N. & Chandrashekar, J. Long distance projections of cortical
1060 pyramidal neurons. *J Neurosci Res* **96**, 1467–1475 (2018).
1061 39. Blanchard, J. W., Victor, M. B. & Tsai, L.-H. Dissecting the complexities of Alzheimer
1062 disease with in vitro models of the human brain. *Nat Rev Neurol* **18**, 25–39 (2022).
1063 40. Sloan, S. A., Andersen, J., Pașca, A. M., Birey, F. & Pașca, S. P. Generation and assembly
1064 of human brain region-specific three-dimensional cultures. *Nat Protoc* **13**, 2062–2085
1065 (2018).
1066 41. Hayward, R. F., Brooks, F. P., 3rd, Yang, S., Gao, S. & Cohen, A. E. Diminishing neuronal
1067 acidification by channelrhodopsins with low proton conduction. *Elife* **12**, (2023).
1068 42. Broussard, G. J. *et al.* In vivo measurement of afferent activity with axon-specific calcium
1069 imaging. *Nat Neurosci* **21**, 1272–1280 (2018).
1070 43. Nicole, O. & Pacary, E. CaMKIIβ in Neuronal Development and Plasticity: An Emerging
1071 Candidate in Brain Diseases. *Int J Mol Sci* **21**, (2020).
1072 44. Vest, R. S., O'Leary, H., Coultrap, S. J., Kindy, M. S. & Bayer, K. U. Effective post-insult
1073 neuroprotection by a novel Ca(2+)/ calmodulin-dependent protein kinase II (CaMKII)

1074 inhibitor. *J Biol Chem* **285**, 20675–20682 (2010).
1075 45. Tsai, L. H., Delalle, I., Caviness, V. S., Jr, Chae, T. & Harlow, E. p35 is a neural-specific
1076 regulatory subunit of cyclin-dependent kinase 5. *Nature* **371**, 419–423 (1994).
1077 46. Chae, T. *et al.* Mice lacking p35, a neuronal specific activator of Cdk5, display cortical
1078 lamination defects, seizures, and adult lethality. *Neuron* **18**, 29–42 (1997).
1079 47. Noble, W. *et al.* Cdk5 is a key factor in tau aggregation and tangle formation in vivo. *Neuron*
1080 **38**, 555–565 (2003).
1081 48. Lee, M. S. *et al.* Neurotoxicity induces cleavage of p35 to p25 by calpain. *Nature* **405**, 360–
1082 364 (2000).
1083 49. Seo, J. *et al.* Activity-dependent p25 generation regulates synaptic plasticity and Aβ-
1084 induced cognitive impairment. *Cell* **157**, 486–498 (2014).
1085 50. Patrick, G. N. *et al.* Conversion of p35 to p25 deregulates Cdk5 activity and promotes
1086 neurodegeneration. *Nature* **402**, 615–622 (1999).
1087 51. Pao, P.-C. & Tsai, L.-H. Three decades of Cdk5. *J Biomed Sci* **28**, 79 (2021).
1088 52. Tsai, L. H., Takahashi, T., Caviness, V. S., Jr & Harlow, E. Activity and expression pattern
1089 of cyclin-dependent kinase 5 in the embryonic mouse nervous system. *Development* **119**,
1090 1029–1040 (1993).
1091 53. Kimura, T., Ishiguro, K. & Hisanaga, S.-I. Physiological and pathological phosphorylation of
1092 tau by Cdk5. *Front Mol Neurosci* **7**, 65 (2014).
1093 54. Nabizadeh, F. *et al.* Neuroimaging Findings of Psychosis in Alzheimer's Disease: A
1094 Systematic Review. *Brain Behav* **15**, e70205 (2025).
1095 55. Sun, N. *et al.* Human microglial state dynamics in Alzheimer's disease progression. *Cell*
1096 **186**, 4386–4403.e29 (2023).
1097 56. Keren-Shaul, H. *et al.* A Unique Microglia Type Associated with Restricting Development of
1098 Alzheimer's Disease. *Cell* **169**, 1276–1290.e17 (2017).
1099 57. Mathys, H. *et al.* Temporal Tracking of Microglia Activation in Neurodegeneration at Single-

1100 Cell Resolution. *Cell Rep* **21**, 366–380 (2017).
1101 58. Olah, M. *et al.* Single cell RNA sequencing of human microglia uncovers a subset
1102 associated with Alzheimer's disease. *Nat Commun* **11**, 6129 (2020).
1103 59. Tuddenham, J. F. *et al.* A cross-disease resource of living human microglia identifies
1104 disease-enriched subsets and tool compounds recapitulating microglial states. *Nat*
1105 *Neurosci* **27**, 2521–2537 (2024).
1106 60. Walker, D. G. *et al.* Patterns of Expression of Purinergic Receptor P2RY12, a Putative
1107 Marker for Non-Activated Microglia, in Aged and Alzheimer's Disease Brains. *Int J Mol Sci*
1108 **21**, (2020).
1109 61. Tsai, A. P. *et al.* Genetic variants of phospholipase C-γ2 alter the phenotype and function of
1110 microglia and confer differential risk for Alzheimer's disease. *Immunity* **56**, 2121–2136.e6
1111 (2023).
1112 62. Ghoreschi, K., Laurence, A. & O'Shea, J. J. Janus kinases in immune cell signaling.
1113 *Immunol Rev* **228**, 273–287 (2009).
1114 63. López-Domínguez, J. A. *et al.* transcript variant 2 is a marker of aging and cellular
1115 senescence. *Aging (Albany NY)* **13**, 13380–13392 (2021).
1116 64. Karabag, D. *et al.* Characterizing microglial senescence: Tau as a key player. *J Neurochem*
1117 **166**, 517–533 (2023).
1118 65. Carling, G. K. *et al.* Alzheimer's disease-linked risk alleles elevate microglial cGAS-
1119 associated senescence and neurodegeneration in a tauopathy model. *Neuron* **112**, 3877–
1120 3896.e8 (2024).
1121 66. Xie, Z. *et al.* Gene Set Knowledge Discovery with Enrichr. *Curr Protoc* **1**, e90 (2021).
1122 67. Huang, B., Lang, X. & Li, X. The role of IL-6/JAK2/STAT3 signaling pathway in cancers.
1123 *Front Oncol* **12**, 1023177 (2022).
1124 68. Puel, A. & Casanova, J.-L. The nature of human IL-6. *J Exp Med* **216**, 1969–1971 (2019).
1125 69. Sun, L. *et al.* Neuroprotection by IFN-γ via astrocyte-secreted IL-6 in acute

1126 neuroinflammation. *Oncotarget* **8**, 40065–40078 (2017).
1127 70. Lyra E Silva, N. M. *et al.* Pro-inflammatory interleukin-6 signaling links cognitive
1128 impairments and peripheral metabolic alterations in Alzheimer's disease. *Transl Psychiatry*
1129 **11**, 251 (2021).
1130 71. Quintanilla, R. A., Orellana, D. I., González-Billault, C. & Maccioni, R. B. Interleukin-6
1131 induces Alzheimer-type phosphorylation of tau protein by deregulating the cdk5/p35
1132 pathway. *Exp Cell Res* **295**, 245–257 (2004).
1133 72. Xiong, X. *et al.* Epigenomic dissection of Alzheimer's disease pinpoints causal variants and
1134 reveals epigenome erosion. *Cell* **186**, 4422–4437.e21 (2023).
1135 73. Finucane, H. K. *et al.* Partitioning heritability by functional annotation using genome-wide
1136 association summary statistics. *Nat Genet* **47**, 1228–1235 (2015).
1137 74. Pooler, A. M., Noble, W. & Hanger, D. P. A role for tau at the synapse in Alzheimer's
1138 disease pathogenesis. *Neuropharmacology* **76 Pt A**, 1–8 (2014).
1139 75. Wu, J. W. *et al.* Neuronal activity enhances tau propagation and tau pathology in vivo. *Nat*
1140 *Neurosci* **19**, 1085–1092 (2016).
1141 76. Gazestani, V. *et al.* Early Alzheimer's disease pathology in human cortex involves transient
1142 cell states. *Cell* **186**, 4438–4453.e23 (2023).
1143 77. Steullet, P. *et al.* Oxidative stress-driven parvalbumin interneuron impairment as a common
1144 mechanism in models of schizophrenia. *Mol Psychiatry* **22**, 936–943 (2017).
1145 78. Wu, W. *et al.* Microglial depletion aggravates the severity of acute and chronic seizures in
1146 mice. *Brain Behav Immun* **89**, 245–255 (2020).
1147 79. Kinoshita, S. & Koyama, R. Pro- and anti-epileptic roles of microglia. *Neural Regen Res* **16**,
1148 1369–1371 (2021).
1149 80. Badimon, A. *et al.* Negative feedback control of neuronal activity by microglia. *Nature* **586**,
1150 417–423 (2020).
1151 81. Chen, Y., Dang, M. & Zhang, Z. Brain mechanisms underlying neuropsychiatric symptoms

1152 in Alzheimer's disease: a systematic review of symptom-general and -specific lesion
1153 patterns. *Mol Neurodegener* **16**, 38 (2021).
1154 82. Garrison, J. R., Fernandez-Egea, E., Zaman, R., Agius, M. & Simons, J. S. Reality
1155 monitoring impairment in schizophrenia reflects specific prefrontal cortex dysfunction.
1156 *Neuroimage Clin* **14**, 260–268 (2017).
1157 83. Seo, J. *et al.* Inhibition of p25/Cdk5 Attenuates Tauopathy in Mouse and iPSC Models of
1158 Frontotemporal Dementia. *J Neurosci* **37**, 9917–9924 (2017).
1159 84. Pao, P.-C. *et al.* A Cdk5-derived peptide inhibits Cdk5/p25 activity and improves
1160 neurodegenerative phenotypes. *Proc Natl Acad Sci U S A* **120**, e2217864120 (2023).
1161 85. Zheng, Y.-L., Li, B.-S., Amin, N. D., Albers, W. & Pant, H. C. A peptide derived from cyclin-
1162 dependent kinase activator (p35) specifically inhibits Cdk5 activity and phosphorylation of
1163 tau protein in transfected cells. *Eur J Biochem* **269**, 4427–4434 (2002).
1164 86. Krivinko, J. M. *et al.* Synaptic Proteome Compensation and Resilience to Psychosis in
1165 Alzheimer's Disease. *Am J Psychiatry* **175**, 999–1009 (2018).
1166 87. Montine, T. J. *et al.* National Institute on Aging-Alzheimer's Association guidelines for the
1167 neuropathologic assessment of Alzheimer's disease: a practical approach. *Acta*
1168 *Neuropathol* **123**, 1–11 (2012).
1169 88. Hyman, B. T. *et al.* National Institute on Aging-Alzheimer's Association guidelines for the
1170 neuropathologic assessment of Alzheimer's disease. *Alzheimers Dement* **8**, 1–13 (2012).
1171 89. McKeith, I. G. *et al.* Diagnosis and management of dementia with Lewy bodies: Fourth
1172 consensus report of the DLB Consortium. *Neurology* **89**, 88–100 (2017).
1173 90. Nelson, P. T. *et al.* Limbic-predominant age-related TDP-43 encephalopathy (LATE):
1174 consensus working group report. *Brain* **142**, 1503–1527 (2019).
1175 91. Zheng, G. X. Y. *et al.* Massively parallel digital transcriptional profiling of single cells. *Nat.*
1176 *Commun.* **8**, 14049 (2017).
1177 92. Hao, Y. *et al.* Integrated analysis of multimodal single-cell data. *Cell* **184**, 3573–3587.e29

1178 (2021).
1179 93. Korsunsky, I. *et al.* Fast, sensitive and accurate integration of single-cell data with
1180 Harmony. *Nat. Methods* **16**, 1289–1296 (2019).
1181 94. McGinnis, C. S., Murrow, L. M. & Gartner, Z. J. DoubletFinder: Doublet Detection in Single-
1182 Cell RNA Sequencing Data Using Artificial Nearest Neighbors. *Cell Syst* **8**, 329–337.e4
1183 (2019).
1184 95. Satpathy, A. T. *et al.* Massively parallel single-cell chromatin landscapes of human immune
1185 cell development and intratumoral T cell exhaustion. *Nat. Biotechnol.* **37**, 925–936 (2019).
1186 96. Granja, J. M. *et al.* ArchR is a scalable software package for integrative single-cell
1187 chromatin accessibility analysis. *Nat. Genet.* **53**, 403–411 (2021).
1188 97. Mathys, H. *et al.* Single-cell transcriptomic analysis of Alzheimer's disease. *Nature* **570**,
1189 332–337 (2019).
1190 98. Zhang, Y. *et al.* Model-based analysis of ChIP-Seq (MACS). *Genome Biol.* **9**, R137 (2008).
1191 99. McLean, C. Y. *et al.* GREAT improves functional interpretation of cis-regulatory regions.
1192 *Nat. Biotechnol.* **28**, 495–501 (2010).
1193 100. Tanigawa, Y., Dyer, E. S. & Bejerano, G. WhichTF is functionally important in your open
1194 chromatin data? *PLoS Comput Biol* **18**, e1010378 (2022).
1195 101. Heinz, S. *et al.* Simple combinations of lineage-determining transcription factors prime cis-
1196 regulatory elements required for macrophage and B cell identities. *Mol. Cell* **38**, 576–589
1197 (2010).
1198 102. Phipson, B. *et al.* propeller: testing for differences in cell type proportions in single cell data.
1199 *Bioinformatics* **38**, 4720–4726 (2022).
1200 103. Ashburner, M. *et al.* Gene Ontology: tool for the unification of biology. *Nat. Genet.* **25**, 25–
1201 29 (2000).
1202 104. The Gene Ontology Consortium. The Gene Ontology Resource: 20 years and still GOing
1203 strong. *Nucleic Acids Res.* **47**, D330–D338 (2019).

1204 105. Chen, E. Y. *et al.* Enrichr: interactive and collaborative HTML5 gene list enrichment
1205 analysis tool. *BMC Bioinformatics* **14**, 128 (2013).
1206 106. Kuleshov, M. V. *et al.* Enrichr: a comprehensive gene set enrichment analysis web server
1207 2016 update. *Nucleic Acids Res.* **44**, W90–7 (2016).
1208 107. Backman, J. D. *et al.* Exome sequencing and analysis of 454,787 UK Biobank participants.
1209 *Nature* **599**, 628–634 (2021).
1210 108. Bellenguez, C. *et al.* New insights into the genetic etiology of Alzheimer's disease and
1211 related dementias. *Nat Genet* **54**, 412–436 (2022).

1212

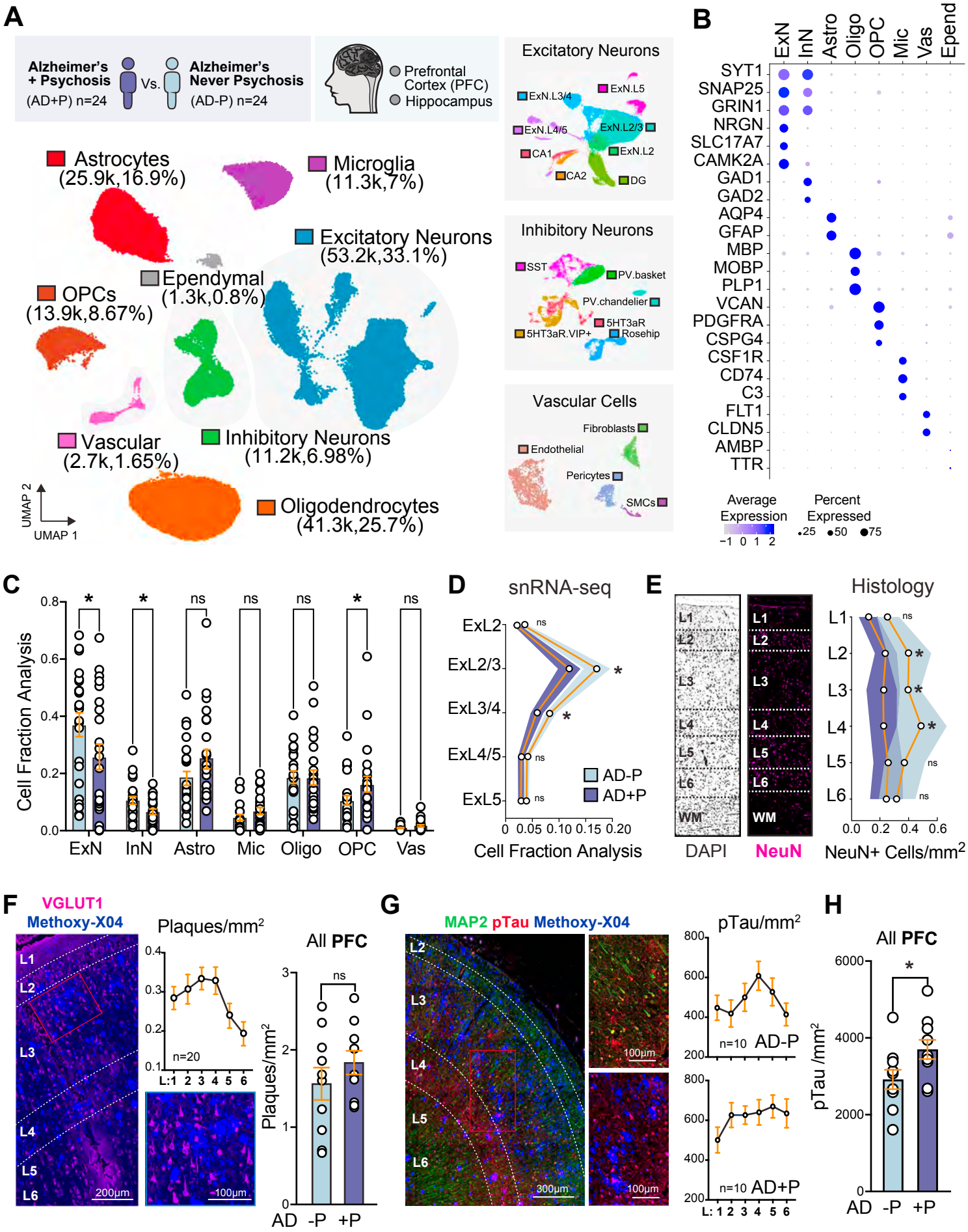


**Figure 1. snRNA-seq atlas of PFC and hippocampus from AD patients with psychosis.**

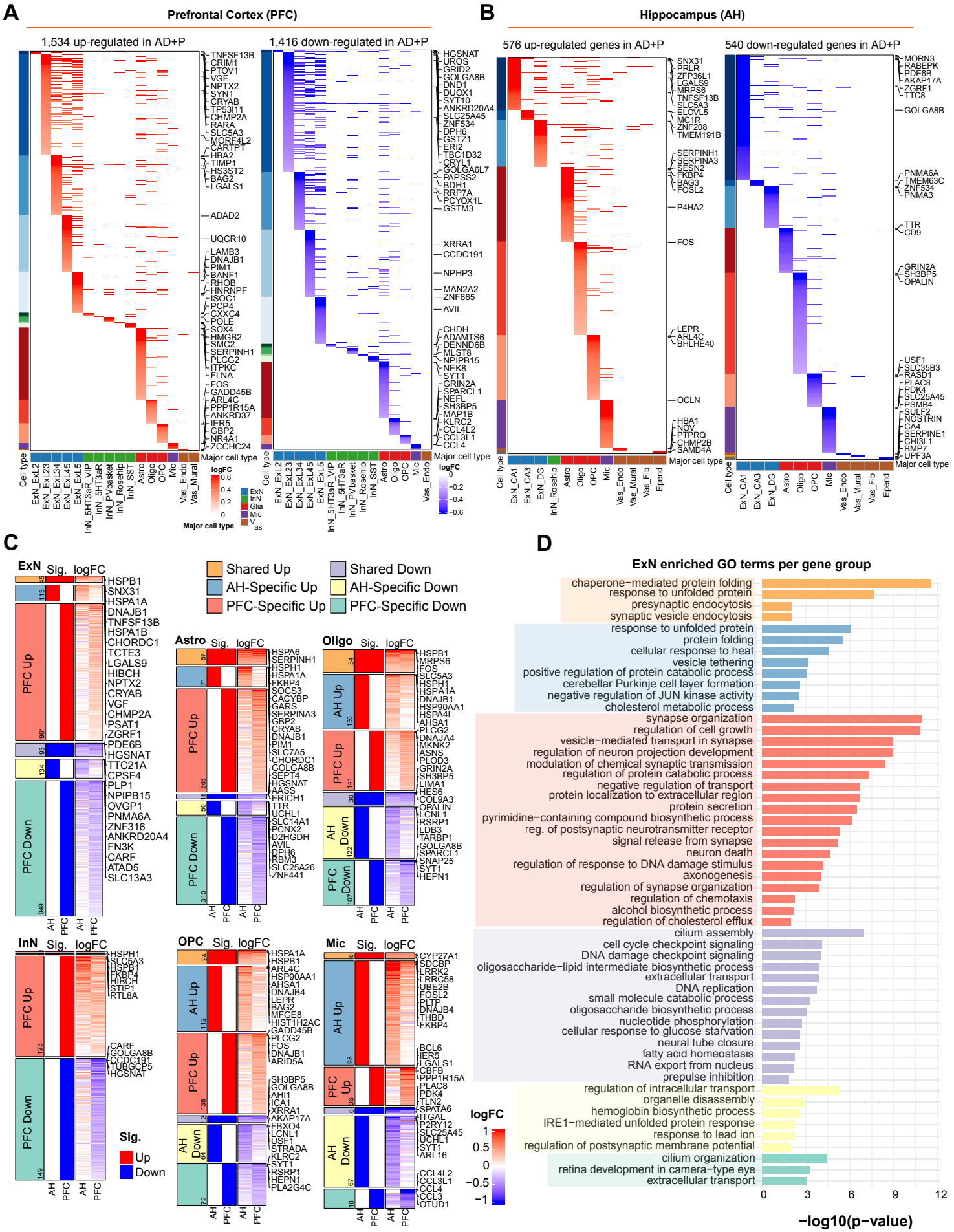


**Figure 2. Cell-type- and brain-region-specific transcriptional changes in AD with psychosis.**

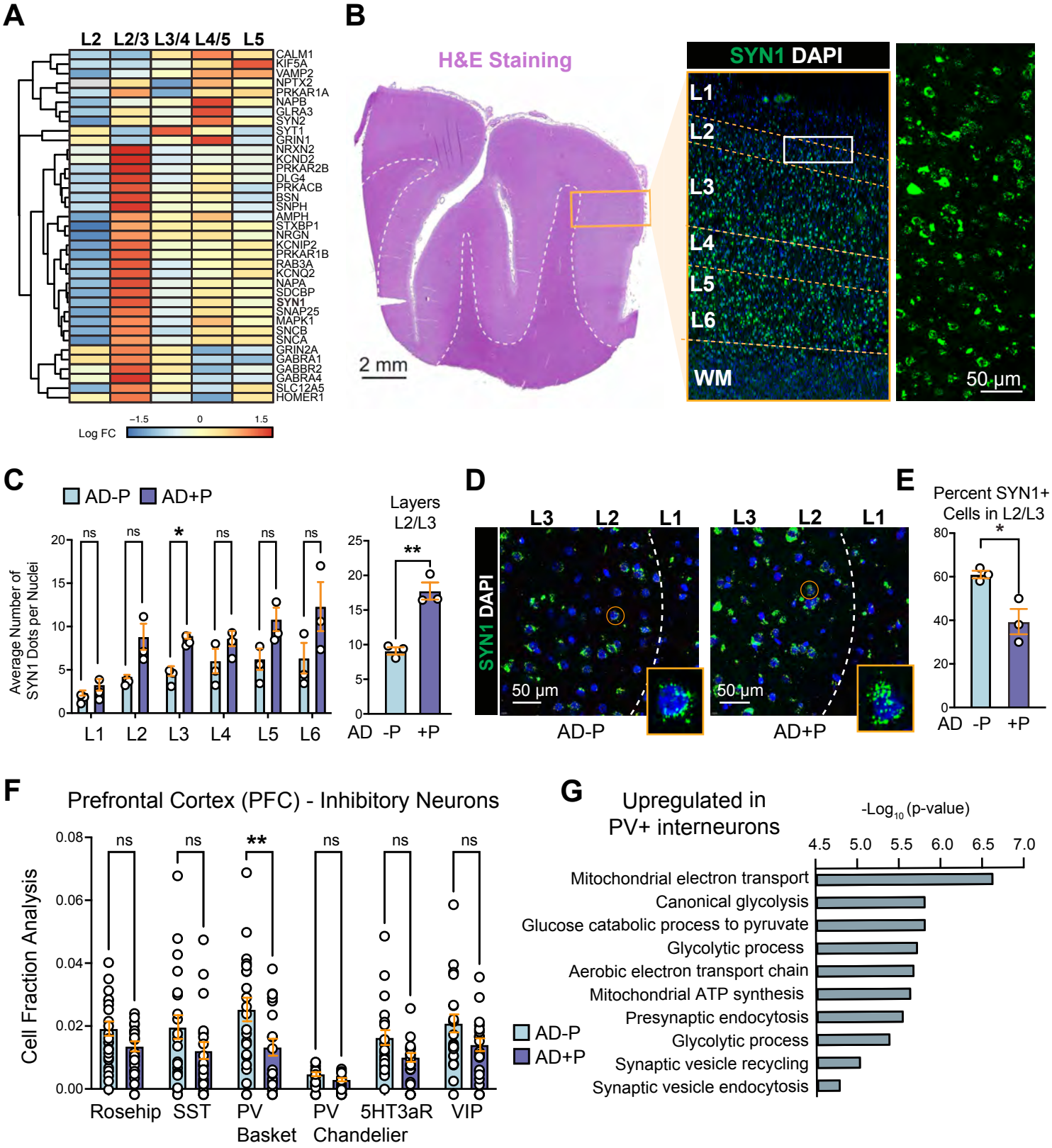


**Figure 3. Upregulation of synaptic-related genes is a compensatory mechanism evoked by surviving excitatory neurons.**

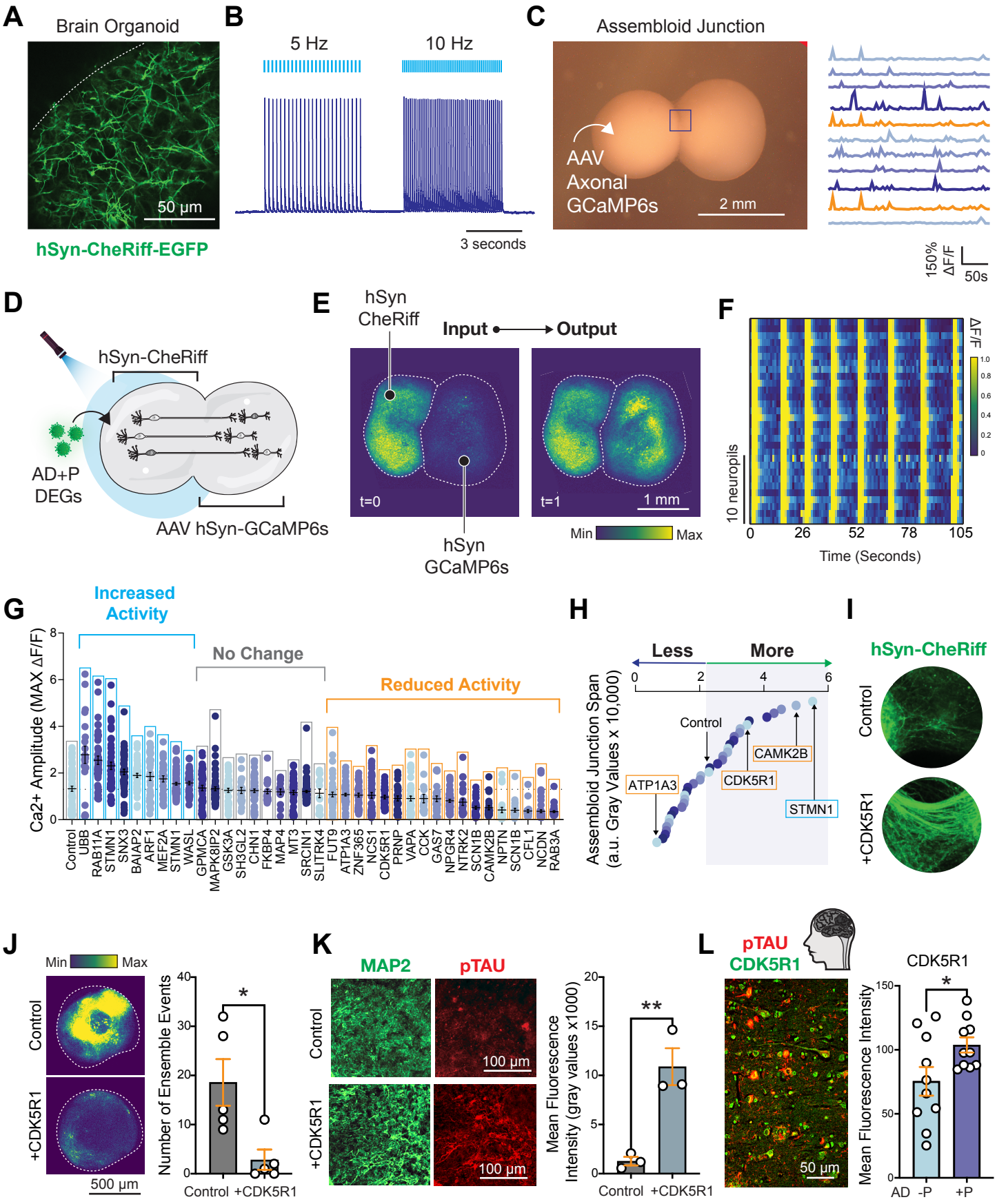


**Figure 4. Functional Characterization of AD+P DEGs from Upper-Layers Excitatory Neurons.**

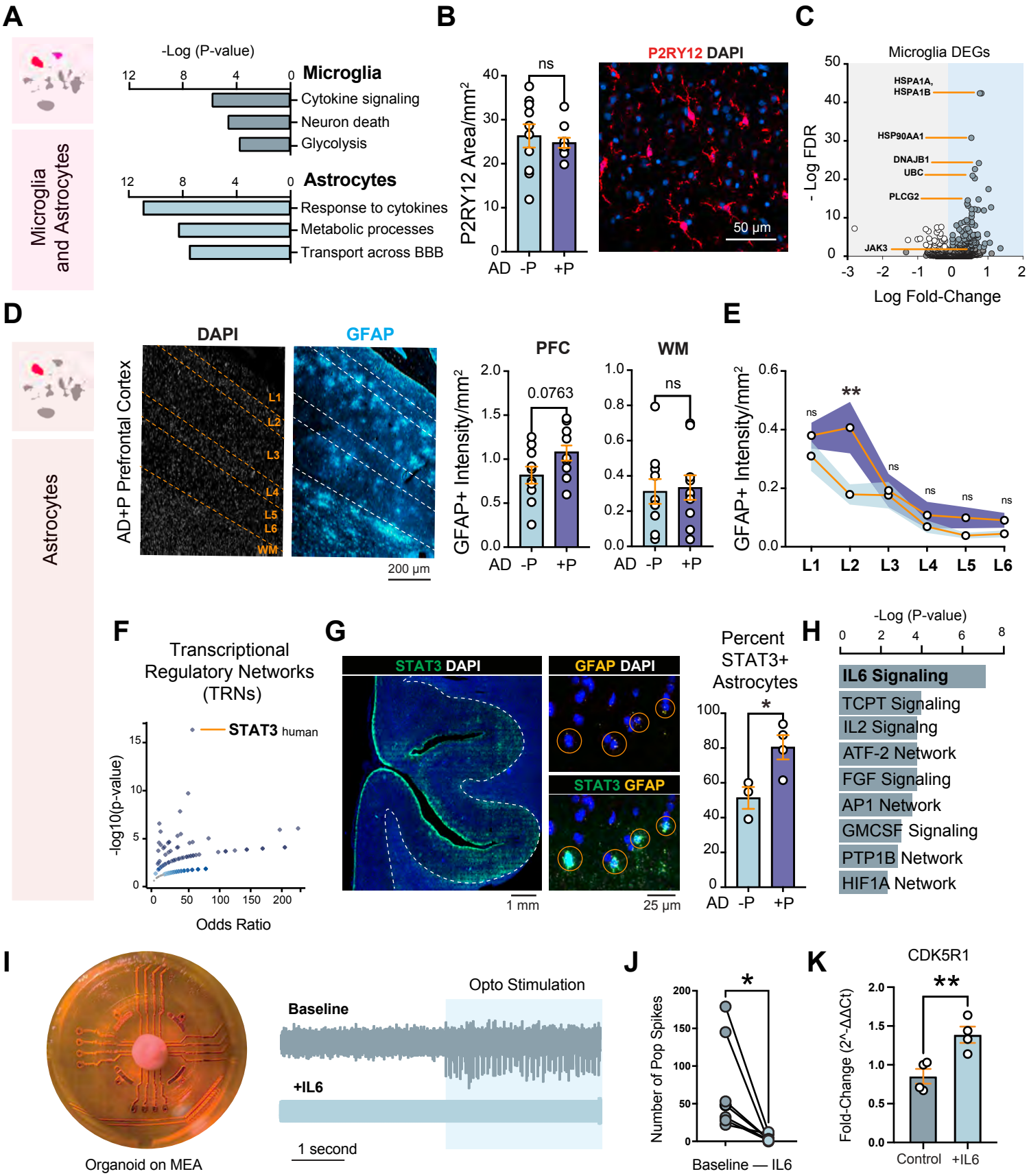


**Figure 5. Glial response in AD+P PFC is marked by microglial exhaustion and astrocyte-driven inflammation.**

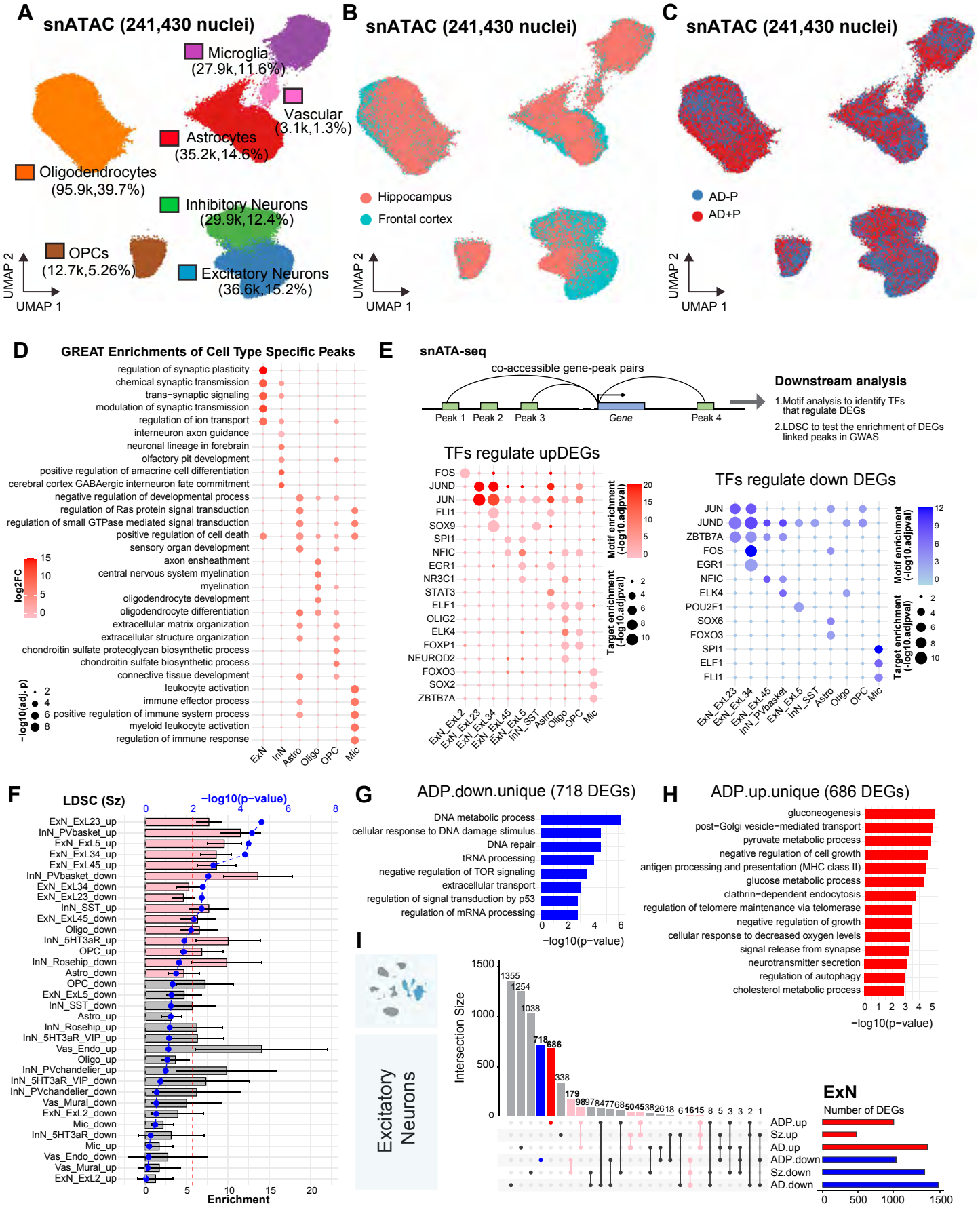


**Figure 6 Epigenetic Regulation of Cell-Type-Specific Gene Expression Changes and Their Association with Schizophrenia Genetics.**